Data processing and analysis of the modulation experiment

Stefanie Javet

Bachelor Thesis in Physics
May 29, 2019

Department of Physics
University of Zurich

Supervisors:

Prof. Dr. Laura Baudis
Adam Brown
Dr. Alessandro Manfredini

Abstract

Radioactive decay is widely assumed to be a stochastic process which cannot be influenced by external conditions. However, in recent years claims on an annual modulation in decay rates of the order $\mathcal{O}(10^{-3})$ have been made. The modulation experiment is designed to investigate the stability of decay rates with time. It contains four identical setups on three different continents to investigate seasonal effects. These locations are Purdue University in the U.S., Nikhef in the Netherlands, Centro Brasileiro de Pesquisas Físicas (CBPF) in Brazil and the University of Zurich in Switzerland. In every location three of the four used sources are monitored with NaI(Tl) detectors. For the Zurich setup, these are ^{54}Mn, ^{60}Co and ^{44}Ti. In this thesis almost one year of data from the Zurich setup was analyzed. The data processing is optimized to obtain reliable decay rates for further analysis. In particular, the spectra are examined for saturated peaks which must be excluded from the analysis. The stability of the detector calibration is verified after some improvements to the calibration algorithm. The analysis procedure was fine-tuned by introducing a background correction for the ^{54}Mn source because of its low decay rate. A statistical framework to search for annual modulation is then introduced with a least squares fitting algorithm. The statistical framework also takes into account possible influences of environmental parameters, which can have an indirect effect on the decay rate by influencing the detection efficiency of the NaI crystals. The performance of the fitting algorithm is investigated with a Monte-Carlo simulation of data sets with and without modulation. The sensitivity is estimated with another Monte-Carlo simulation. At the end, for every monoenergetic line in the data of the Zurich setup, a limit on the modulation amplitude is found, which is consistent with the sensitivity. In the ^{60}Co decay an amplitude limit of $2.7 \cdot 10^{-3}$ is set.

Contents

Acknowledgements

I would like to thank Prof. Dr. Laura Baudis for the opportunity to write this thesis in her group. Further, I would like to thank Adam Brown for his support and knowledge during the entire work process. I would also like to thank Dr. Alessandro Manfredini for his help with the statistical analysis. Both have patiently answered my many questions and expanded my knowledge horizon.
Secondly, I would like to thank my family and friends for the support while doing this thesis.

1. Introduction

It is widely assumed that radioactive decay is a spontaneous process which can be defined only using the half-life, which is a characteristic of a particular isotope. It is impossible to predict which nucleus will decay next, only the number of nuclei which decay in a given time can be estimated. Radioactive decay cannot be influenced by external conditions such as temperature or pressure [1]. In recent years Jenkins et al. [2] claimed an annual modulation in the radioactive decay of long-lived isotopes which is correlated with the Earth-Sun distance. There are also other papers [3, 4] which support the theory of Jenkins et al. [2]. The claimed annual variations are of the order $\mathcal{O}(10^{-3})$.

Papers also exist which reject modulation of decay rates. Norman et al. [5] refute the correlation between decay rates and the Earth-Sun distance and also set limits on a possible modulation amplitude which are of the order $\mathcal{O}(10^{-4})$. Others have also found evidence for no modulation in decay rates [6, 7].

The modulation experiment was constructed to re-examine the idea of an annual modulation in long-lived radioactive decays. The experiment consists of four setups located on three different continents. In this experiment not only the decay rate is measured, but also external parameters such as temperature, pressure and radon level are measured and documented. With these values, changes in the decay rate can be related to systematic influences.

The experimental setup at Zurich has been taking data with eight NaI(Tl) detectors for almost two years. The goal of this thesis is to perform a first analysis on the Zurich data set. In the first step of analysis the data have to be processed, to obtain decay rates from the raw waveforms. Chapter 4 describes this processing including some modifications which were needed to achieve stable performance on the one year of Zurich data. In chapter 5 the further analysis of this data is presented, which results in a limit on the amplitude of modulation allowed by these data.

2. Theory

2.1. Radioactive decay

If a nucleus is stable it can not convert spontaneously into another nucleus. But if a nucleus is unstable it can decay after a finite time into other nuclei while emitting α-particles, electrons or positrons or it can decay through fission. Finally, a nucleus can decay from an excited state into its ground state while emitting γ-rays. A necessary but not sufficient condition for a nucleus to decay is that the mass of the nucleus is larger than the sum of the masses of the decay products.

$$M({}^{A}_{Z}X) \geq M({}^{A'}_{Z'}Y) + M_2 \tag{2.1}$$

${}^{A}_{Z}X$ is a particular nucleus with atomic number Z and mass number A. ${}^{A'}_{Z'}Y$ is the nucleus to which ${}^{A}_{Z}X$ decays and M_2 is the mass of the emitted α-particle, electron, positron or second fission product. Ever if this condition is fulfilled spontaneous decay can be prevented by a potential barrier or symmetry conditions.
Radioactive decay is a spontaneous process which can be described by an exponential decay law. The probability that a particle decays is equally likely per unit time for every nucleus of the same isotope. The activity A of a source with N radioactive nuclei is

$$A = -\frac{dN}{dt} = \lambda N \tag{2.2}$$

where λ is the decay constant, or the decay probability for single nucleus per unit time. Through integration we get the activity at the time t.

$$A(t) = A_0 e^{-\lambda t} \tag{2.3}$$

A radioactive isotope can be characterized by its half-life. This is the time after which half of the unstable nuclei have decayed.

$$\tau = \frac{1}{\lambda} \qquad\qquad t_{1/2} = \tau \cdot \ln 2 \tag{2.4}$$

where τ is the mean lifetime of a radioactive particle before decay [8].
As mentioned at the beginning of this chapter there are various types of radioactive decay. The endpoint of a radioactive decay is a stable state. This can be achieved through alpha decay, beta decay, gamma decay, electron capture, internal conversion or nuclear fission. Because in the modulation experiment only beta decay, electron capture and gamma decay are relevant, these three decay modes are discussed more closely in the following.

2.2. Beta decay

β^- decay is the conversion of a neutron into a proton, while emitting an electron and a electron antineutrino:

$$ {}^{A}_{Z}X \rightarrow {}^{A}_{Z+1}\,Y + e^- + \bar{\nu}_e \tag{2.5} $$

where the atomic number Z gives the number of protons, the mass number A is the number of nucleons in the nucleus which is the sum of protons and neutrons. X and Y stand for the respective element. This decay is energetically possible if the mass of the daughter atom is smaller than the mass of its isobaric neighbor [9].

$$ M(A, Z) > M(A, Z + 1) \tag{2.6} $$

This is the case if a neutron at the Fermi edge can get into a lower unoccupied proton level after converting into a proton. The produced electron and antineutrino leave the nucleus after their formation [8].

β^+ decay is the opposite process of the β^- decay. It is characterized by the conversion of a proton in a neutron, while emitting a positron and a electron neutrino:

$$ {}^{A}_{Z}X \rightarrow {}^{A}_{Z-1}\,Y + e^+ + \nu_e \tag{2.7} $$

This decay is possible if the mass of the parent atom is at least $2m_e$ greater than that of the daughter:

$$ M(A, Z) > M(A, Z - 1) + 2m_e \tag{2.8} $$

Where m_e is the mass of the electron [9]. This relation is fulfilled if, because of the conversion, the new neutron can occupy a lower energy level than the proton was in. If that is the case the binding energy of the daughter nucleus is larger than that of the parent nucleus. This excess of energy is released as kinetic energy of the positron and neutrino emitted in this process.
A characteristic of β^+ decay is that the emitted positron annihilates with an electron after having been slowed down. This process emits two photons in opposite directions with an energy of 511 keV [8].

2.3. Electron capture

In electron capture an atomic electron from one of its atomic shells is captured and reacts with a proton to create a neutron, while an electron neutrino is emitted.

$$ {}^{A}_{Z}X + e^- \rightarrow {}^{A}_{Z-1}\,Y + \nu_e \tag{2.9} $$

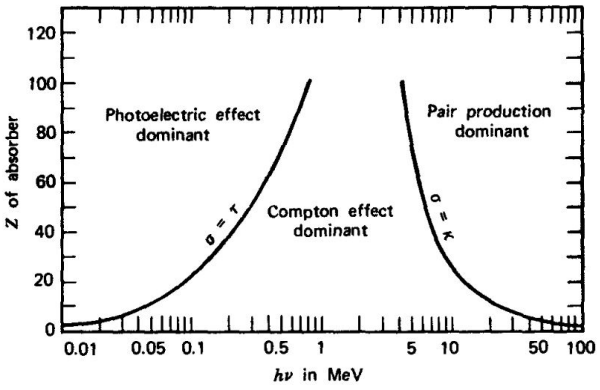

Figure 1: The three types of γ-ray interaction and their probability of occurrence as a function of Z of the absorber material and the incident γ-ray's energy. The lines show the values where the two neighboring processes are equally probable [10].

Most of the time this electron comes from the K-shell, the innermost shell of the atom. In this process a vacancy is produced in this low energy shell in which an electron from a higher shell can fall down while emitting characteristic X-rays [8]. The condition that this decay is possible is

$$M(A, Z) > M(A, Z-1) + \varepsilon/c^2 \tag{2.10}$$

where ε is the excitation energy of the atomic shell of the captured electron [9].

2.4. Gamma decay

The nucleus can be described with a shell model. The nucleons are able to occupy discrete energy states inside the nucleus. If a nucleon is left in an higher energy state after an α- or β decay the nucleus is excited. This nucleon can de-excite into a lower energy state by emitting electromagnetic radiation, which is called γ-radiation. The excited nucleus decays by γ-decay into its ground state [9, 1]:

$$^A_Z X^* \rightarrow ^A_Z X + \gamma \tag{2.11}$$

2.5. Gamma-ray interactions

To explain the mechanism of operation of the detector used in the modulation experiment three kinds of γ-ray interactions are introduced: the photoelectric effect, Compton scattering and pair production. These three processes lead to the

total or partial transfer of photon kinetic energy to electron kinetic energy. It is through these three processes that energy is deposited in the NaI(Tl) crystals. The probability of the three γ-ray interactions in values of the atomic number Z and the γ-ray energy are shown in figure 1.

2.5.1. Photoelectric absorption

In photoelectric absorption a photon interacts with an atom which absorbs the full energy of the photon and ejects a photoelectron. This interaction cannot happen with a free electron. Because of the energy and momentum conservation a third reaction partner, the nucleus which takes the recoil energy, is needed. In most cases, if the photon has sufficient energy, the photoelectron is ejected from the K-shell of the atom. It has an energy given by the difference of the energy of the incident photon $E_\gamma = h\nu$ (h is Planck's constant and ν is the frequency) and its original binding energy E_b [10].

$$E_{e^-} = h\nu - E_b \tag{2.12}$$

After the photoelectron is emitted a vacancy is created in the shell from which the photoelectron came. This vacancy is quickly filled by an electron from a higher shell and X-rays are emitted to release the energy difference between the two shells. These characteristic X-rays have an energy which can be described by *Moseley's law*

$$E = Ry(Z-1)^2\left(\frac{1}{n^2} - \frac{1}{m^2}\right) \tag{2.13}$$

where $Ry = 13.6$ eV is the Rydberg's constant, n and m are the principal quantum numbers and Z is the atomic number. If this energy is transferred to an electron from the same atom instead, and the energy is larger than the binding energy, the electron can be emitted and is called an *Auger electron* [11].
The photoelectric process is the most likely with γ-rays of relatively low energy, as shown in figure 1. The cross-section of photoelectric absorption is proportional to a power of the atomic number Z:

$$\sigma \cong constant \times \frac{Z^n}{E_\gamma^{3.5}} \tag{2.14}$$

where n varies between 4 and 5 with respect to the energy of the incident photon [10].

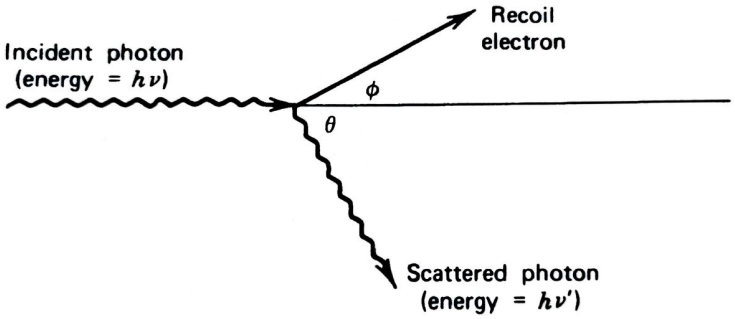

Figure 2: Compton scattering. Figure from [10].

2.5.2. Compton effect

The Compton effect is a process where an incident γ-ray scatters off a free or outer-shell electron as shown in figure 2.
In the process the recoil electron absorbs some of the energy of the photon which can be written in terms of the scattering angle θ:

$$h\nu' = \frac{h\nu}{1 + \frac{h\nu}{m_0c^2}(1 - \cos\theta)} \tag{2.15}$$

where m_0c^2 is the rest mass energy of the electron. If the scattering angle is very small the recoil electron gains very little energy and the scattered photon has almost the same energy as the incident photon. The other extreme, when the scattering angle is the maximum $\theta = \pi$, is known as backscattering. In this case the electron recoils in the incident photon's direction, and the maximum possible energy is transferred to the electron. The differential scattering cross section gives the differential probability of Compton scattering and is described by the *Klein-Nishina formula*:

$$\frac{d\sigma}{d\Omega} = Zr_0^2 \left(\frac{1}{1 + \alpha(1 - \cos\theta)}\right)^2 \left(\frac{1 + \cos^2\theta}{2}\right) \left(1 + \frac{\alpha^2(1 - \cos\theta)^2}{(1 + \cos^2\theta)(1 + \alpha(1 - \cos\theta))}\right) \tag{2.16}$$

where $\alpha = h\nu/m_0c^2$ and r_0 is the classical electron radius [10].

2.5.3. Pair production

Pair production happens near a nucleus, and involves the conversion of an incident photon into an electron-positron pair. For this process to be possible the incident

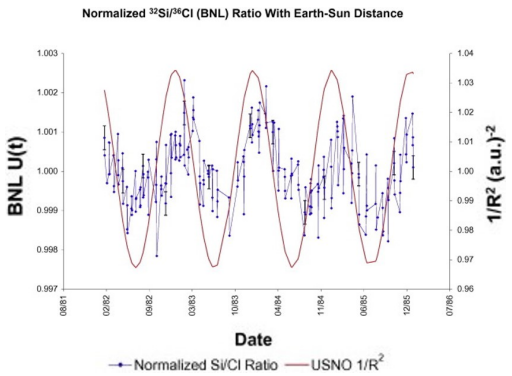

(a) The plot of $U(t)$ for the $^{32}Si/^{36}Cl$ ratio with $1/R^2$ where R is the Earth-Sun distance

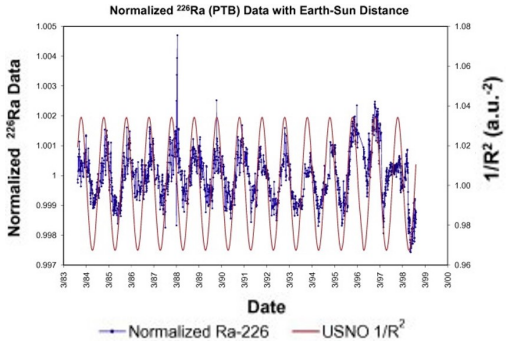

(b) Plot of $U(t)$ for the PTB data with the source ^{226}Ra along with the $1/R^2$ plot where R is the Earth-Sun distance

Figure 3: Plots of different sources where Jenkins et al. [2] claim that the radioactive decay rates shows an annual modulation which is correlated with the Earth-Sun distance. From [2].

γ-ray must have a minimum energy of $2m_ec^2 = 1.02$ MeV which corresponds to the combined rest energy of the two emitted particles. Almost all energy above this threshold is given to the electron-positron pair as kinetic energy.

$$E_{e^-} + E_{e^+} = h\nu - 2m_ec^2 \tag{2.17}$$

Once the positron has slowed down it annihilates into two photons with an energy of 511 keV each. The cross-section magnitude is proportional to the square of the atomic number of the absorber [10].

$$\sigma \propto Z^2 \tag{2.18}$$

2.6. Modulation in decay rates

In 1896 Becquerel discovered radioactivity. A lot of experiments have shown that the decay rate are not affected by external influences such as temperature, pressure, magnetic fields or chemical composition [1]. There is no theoretical basis for an annual modulation of radioactive decay rates.
However, in recent years various publications have claimed that the decay rate is influenced by the Sun-Earth distance. Jenkins et al. [2] published an article in which the fluctuations in β decay rates are correlated in time with the distance between the Earth and the Sun. For their analysis they used data from the Brookhaven

National Laboratory (BNL) where the half-life of ^{32}Si was measured between 1982 and 1986 [12]. A long-lived comparison standard ^{36}Cl was also measured simultaneously in the same detector. The decay rate of ^{36}Cl with a half-life of $T_{1/2} = 3.01 \times 10^5$ y was assumed to be constant. By computing the ratio between the activity of the two sources $^{32}Si/^{36}Cl \equiv A(^{32}Si)/A(^{36}Cl)$ systematic effects should have cancelled. The time independent function $U(t) \equiv [A(t)/A(0)] \exp(+\lambda t)$ was calculated to allow the result to be compared with results from experiments with different sources. Figure 3a shows the plot of the function $U(t)$ along with a plot of $1/R^2$ where R is the Earth-Sun distance. They claim that annual modulation is evident from the plot and that the formal probability that this correlation would arise from two uncorrelated data sets is 6×10^{-18}.
Jenkins et al. [2] also analyzed data from the Physikalische-Technische Bundesandstalt (PTB) where the half-life of ^{226}Ra was measured. The long-lived comparison in this case was ^{152}Eu and the experiment took data over 15 years. Also in this data set they found evidence for annual modulation as shown in figure 3b. The formal probability that this correlation could arise from two uncorrelated data sets is 2×10^{-246}. The relative amplitude of the modulation is 1.5×10^{-3} [2].

There are several other papers which claim variations in the decay rate. Parkhomov [4] investigated the decay rates of ^{60}Co and ^{90}Sr-^{90}Y over 10 years. They found annual modulation with an amplitude of 0.3%. Alexeyev et al. [3] collected data over two years of the ^{214}Po decay. They found an amplitude for annual modulation which is $(8.9 \pm 2.3) \times 10^{-4}$.

In response to the paper of Jenkins et al. [2], Norman et al. [5] analyzed data they had collected over 15 years in three different experiments which were designed to measure the half-lives of ^{44}Ti, ^{108m}Ag and ^{121m}Sn. ^{22}Na, ^{133}Ba, and ^{241}Am are used as reference sources to minimize the influence of variations in the detector or electronics performance. They statistically analyzed the data for a null hypothesis (no annual modulation) and a modulation hypothesis with an amplitude of 0.15%. In all cases the null hypothesis was strongly favored over the modulation hypothesis. Using these results Norman et al. [5] claimed that there is no evidence for correlations between the rates of decay of ^{44}Ti, ^{108m}Ag or ^{121m}Sn and the Earth-Sun distance. They also set limits on the maximum possible amplitude of modulation which are 0.06% for ^{22}Na/^{44}Ti, 0.024% for ^{241}Am/^{121m}Sn and 0.004% for ^{133}Ba/^{108m}Ag. With these results they rejected the theory of modulation from Jenkins et al. [2].

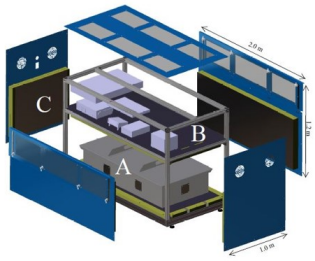

Figure 4: A schematic of a single box for the modulation experiment.

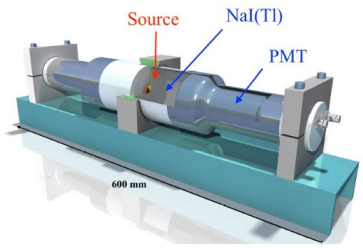

Figure 5: One channel of the experiment, containing a radioactive source between two NaI(Tl) detectors.

3. Experiment

The modulation experiment is constructed to investigate the stability of radioactive decay rates with time. All used sources decay via a β decay. The emitted γ-rays of the de-excited nucleus are measured with a sodium iodide scintillator coupled to a photomultiplier tube (PMT).

3.1. Experimental setup

Four identical setups are distributed over three different continents to investigate seasonal influences. These locations are Purdue University in the U.S., Nikhef in the Netherlands, Centro Brasileiro de Pesquisas Físicas (CBPF) in Brazil and the University of Zurich in Switzerland. Each isotope used in the experiment is monitored in at least two locations. The isotopes are ^{54}Mn, ^{60}Co, ^{137}Cs and ^{44}Ti. Their locations and half lives are shown in table 1.

Source	Half Life	Ref.	Institute			
^{44}Ti	59.1(3) y	[14]	CBPF	Nikhef	Purdue	Zurich
^{54}Mn	312.2(2) d	[15]			Purdue	Zurich
^{60}Co	5.271(4) y	[16]	CBPF	Nikhef	Purdue	Zurich
^{137}Cs	30.08(9) y	[17]	CBPF	Nikhef		

Table 1: Overview of the radioactive isotopes used in the experiment and their location [13].

A sketch of a single setup box is shown in figure 4. On the lower rack (A) the detectors and the sources are stored. To keep their temperature stabilized the

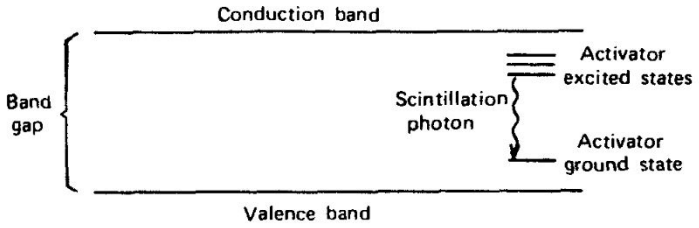

Figure 6: Band structure of a doped crystal in a scintillator [10].

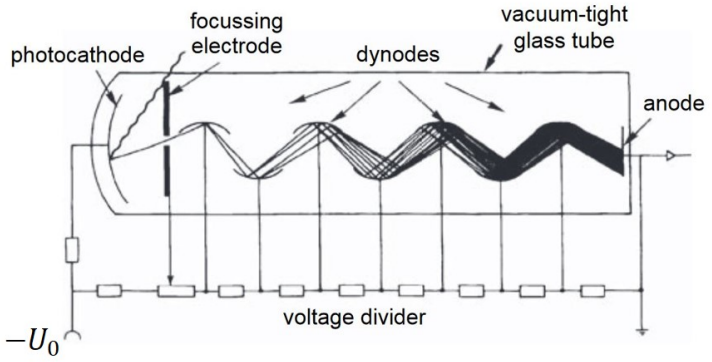

Figure 7: A schematic picture of a photomultiplier tube (PMT). An incident photon emits photoelectrons at the photocathode. These photoelectrons are focussed and accelerated by the electric field and multiplied at the dynodes. The amplified electrons are collected at the anode and the signal, which is proportional to the incident photon energy, is measured [11].

inner box is thermally insulated by a 10 cm thick layer of polyurethane foam (C) and a heater is used to actively stabilize the temperature. The air cooled top rack (B) contains all the electronics and data acquisition system. In figure 5 one channel is shown. Each source is between two cylindrical 3" × 3" NaI(Tl) crystals coupled to photomultiplier tubes (PMTs). Each detector pair is shielded from its neighbours by 5 cm of lead. The box contains four pairs of NaI(Tl) detectors, and one pair is measuring the background. In addition each detector is equipped with a LED for deadtime measurements and to investigate the efficiency of the whole measurement [13].

3.2. NaI(Tl) detector with photomultiplier tube

The detectors used in the modulation experiment contain a NaI(Tl) scintillator crystal. An emitted γ-ray from the radioactive decay of a source can interact with

the crystal through photoelectric absorption, Compton scattering or pair production. The production of electron-hole pairs excite the crystal. Photons in the visible spectrum, in sodium iodide the most likely wavelength is 415 nm [11], are emitted in the deexcitation process. The photomultiplier tube (PMT) counts the scintillation photons, the number of which is proportional to the incident γ-ray's energy.

The scintillator used in the modulation experiment is an inorganic sodium iodide crystal, doped with thallium. In a crystal lattice of an insulator or semiconductor, electrons only have discrete bands of energy available. As shown in figure 6 the lower energy band is called valence band and represents electrons that are essentially bound at lattice sites. This band is normally fully occupied. The other band is the conduction band which is normally empty and separated from the valence band by an energy known as the band gap, usually about 3 eV to 10 eV [11]. When a γ-ray interacts with the crystal the electron off which it scatters or is absorbed, while passing through the crystal, excites electrons from the valence band into the conduction band. A hole is left in the valence band. The electron in the conduction band can move freely through the crystal lattice. Because the return of an electron into the valence band with the emission of a photon is inefficient the crystal is doped with an activator in this case, thallium. This activator creates energy states inside the band gap. When the hole, created by the excited electron, drifts to the location of an activator it ionizes it. An electron in the conduction band can drop into an activator energy state and then deexcite into the ground state of the activator. During the deexcitation a photon in the visible spectrum is emitted [10].
An incident γ-ray with energy E_{kin} creates a specific number of photons N_{ph} with energy $h\nu$ in the scintillator through the mechanism described above:

$$N_{ph} = \delta \cdot E_{kin}/h\nu \tag{3.1}$$

$\delta < 1$ is the efficiency of the scintillating material. Of these, N_{ph} photons only a fraction β reaches the photocathode of the PMT because they can be absorbed before reaching the photocathode [8].

In figure 7 a schematic picture of a PMT is shown. On the photocathode photoelectrons are emitted by the photoelectric effect. They are focussed and accelerated by the electric field to the first dynode. There the electrons are multiplied by the emission of secondary electrons. This process happens at every dynode until the secondary electrons from last dynode are collected at the anode and produce a measurable signal.
The number of photoelectrons produced at the photocathode depends on the quantum efficiency of the PMT. This parameter gives the probability of an emitted

photoelectron per incident photon at the photocathode and depends on the wavelength of the incoming photon [11].
For a PMT with n dynodes and a secondary emission coefficient g the current amplification is

$$A = g^n \tag{3.2}$$

A single photoelectron can be amplified with a factor of $\sim 10^7$ [18], depending on the number of stages.

3.3. Data acquisition

Each event is stored individually in the form of the full voltage trace (waveform) using a custom data acquisition system (DAQ). The analog-to-digital converter (ADC) used is able to sample up to 16 channels with a 14 bit range and a voltage range of 2V. A waveform is stored if the following three trigger conditions are fulfilled:

- The current bin has to be greater than the previous bin
- A specific threshold voltage has been passed which is set as the voltage corresponding to an energy of $\sim$ 100 keV
- The previous event should not be within $\sim$ 7 times the NaI(Tl) decay time (1.6μs) [13] to minimize the occurrence of pile up events

To monitor the efficiency of the setup each detector is equipped with an LED. The LED consistently pulses at a rate of $\sim$ 50 Hz. The waveforms of the detected LED pulses are flagged and stored exactly like real event for further analysis.

In addition to the waveforms, slow control parameters are also stored. This includes the temperature, pressure, humidity, magnetic field, high voltage and radon activity [13].

To be sure that we only analyze properly-recorded events every event gets an error code in the form of Bits. If this error code is 0 the event is considered good. Error code 1 is set if the amplitude of the event is sufficiently large that it is saturated. This means that the peak is higher than the 2V range of the ADC. Error code 2 means that the root mean square (RMS) of the baseline is unusually high, which can affect the energy reconstruction for that event. If there is a double peak structure in the waveform consistent with multiple hits error code 4 is set. The bitwise combination of error codes is possible if more than one apply to an event.

Source	Channel number	Peak 1 [kev]	Peak 2 [kev]	Peak 3 [kev]
^{60}Co	0, 1	1173.2	1332.5	2505.7
^{54}Mn	2, 3	834.8		
^{44}Ti	4, 5	511.00	1157.02	1668.02
Background	6, 7	1460		

Table 2: Energy of peaks found in the spectra of the different sources in the Zurich experiment.

3.4. Sources

The sources used in the Zurich detectors are ^{60}Co, ^{54}Mn and ^{44}Ti. They are arranged in channels numbered from 0 to 7. In table 2 the channel numbers of the sources are shown. Every source has two channels because the source is between two detectors.
To analyze the decay rate of a particular source the energy of the emitted γ-rays has to be known. In figure 8 the decay scheme and an example spectrum is shown. For each of the sources used in Zurich figure 8a shows that ^{60}Co decays in 99.88% of cases by β^- decay into an excited state of ^{60}Ni. To get from this excited state into the ground state ^{60}Ni emits two γ-rays with an energy of 1.1732 MeV and 1.3325 MeV. In just 0.12% of the cases ^{60}Co decays by β^- decay into a lower excited state of ^{60}Ni where just one γ-ray with an energy of 1.3325 MeV is emitted [16]. These energy peaks are shown in the spectrum of ^{60}Co in figure 8b recorded by modulation experiment in Zurich.
^{54}Mn decays 100% by electron capture into an excited state of ^{54}Cr which emits a γ-ray of 834.8 keV to reach the ground state [15]. This can be seen in figure 8c.
In figure 8e the decay of ^{44}Ti by electron capture into an excited state of ^{44}Sc is shown. ^{44}Sc emits two γ-rays at 78.337 keV and 67.875 keV to get into its ground state before it decays, again by β^+ decay, into an excited state of ^{44}Ca. There a γ-ray with an energy of 1157.02 keV is emitted to get into the ground state [14]. Because of the β^+ decay the spectrum in figure 8f contains a peak at 511 keV, from the annihilation of the emitted positron, in addition to the peaks from the γ decays.
The spectra of ^{60}Co and ^{44}Ti also each contain a third peak at the sum of the two other peaks. These peaks come from events where both γ-rays reach the detector at the same time. Table 2 summarizes the energy of the peaks visible from the sources used in Zurich. The peak at 1460 keV from ^{40}K contamination in the background channel is also shown.

A spectrum from a γ-ray detector has several components beside full absorption

peaks. The edge immediately to the left of the peak, which is best visible in figure 8d, is called the *Compton edge*. The spectrum body below this Compton edge is called the *Compton continuum*. It contains every energy of the recoil electron from Compton scattering by an angle from 0 to π. The peak around 0.25 Mev which can be seen on top of this Compton continuum is the so called *backscatter peak*. This backscatter peak is caused by the Compton scattering of γ-rays off the detector shielding material. If Compton scattering happens with an angle greater than about 120° the scattered photon always has an almost identical energy of 0.25 MeV or less. If the photon with this energy of about 0.25 MeV scatters back into the detector it causes this peak. Because ^{54}Mn has only one emitted γ the backscatter peak is clearly visible, but the process happens for all sources [10].

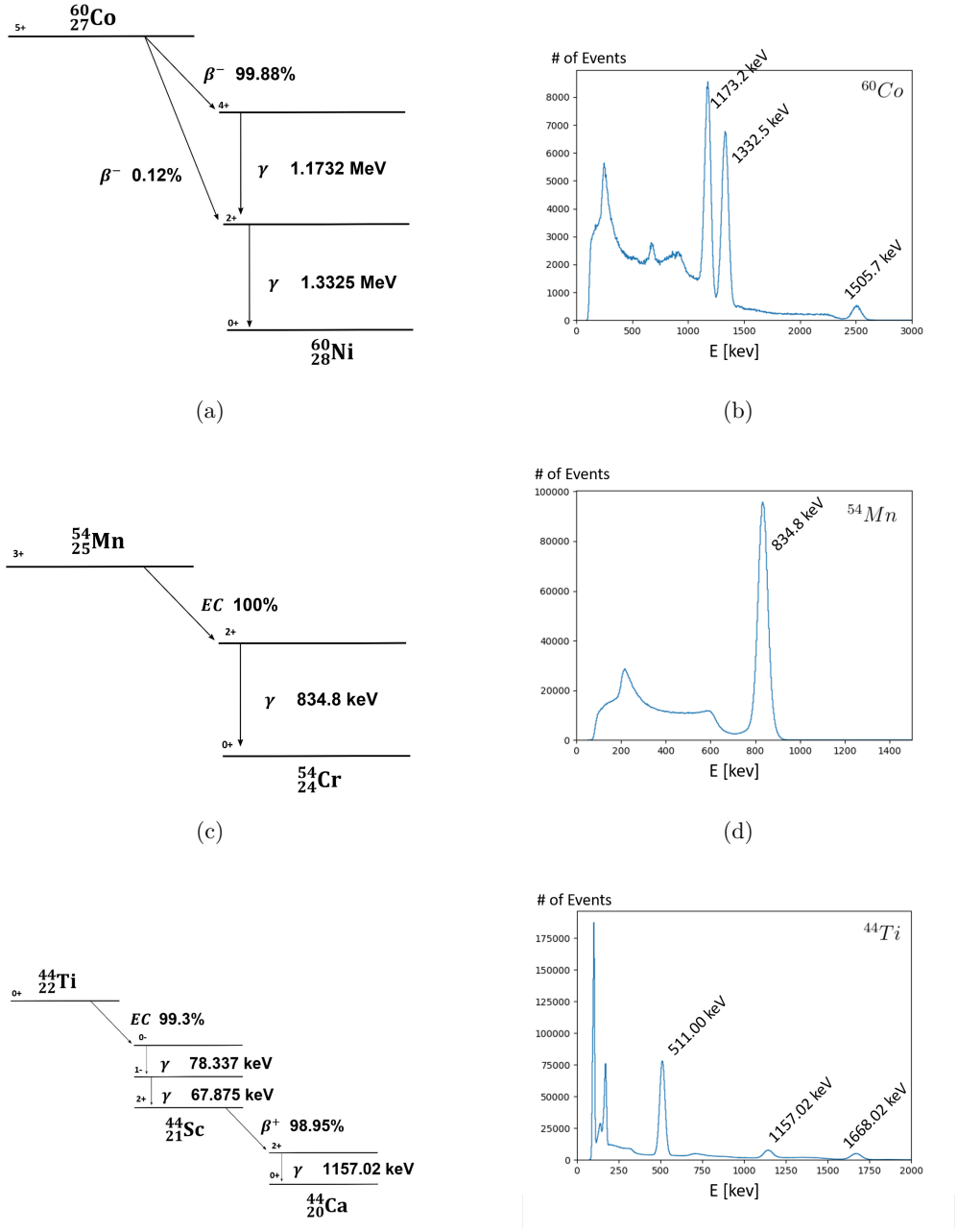

Figure 8: Left: the decay schemes of (a) ^{60}Co [16], (b) ^{54}Mn [15] and (c) ^{44}Ti [14]. Right: the spectrum corresponding to each source as seen by the modulation experiment in Zurich.

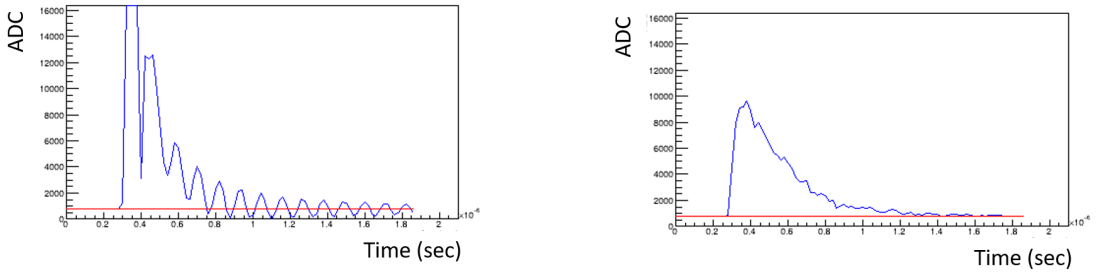

(a) Waveform of an event with error code 1

(b) waveform with error code 0

Figure 9: Waveform with overflow (left) and a normal pulse (right) as seen in a NaI(Tl) detector.

4. Data Processing

4.1. Processing pipeline

To process data from the raw waveform to decay rates some steps are needed. This steps are done with a processing script called *daqana* written by the collaboration. In some steps of this processing improvements are made or the results are verified. In the next few subsections the method to optimize the data processing pipeline to get a good data set which can be analyzed is explained.

The first step is to integrate the waveform to get an uncalibrated spectrum of events. Also some other information are taken and stored such as to which channel the event belongs, the amplitude of the peak and of course the time at which the event happened. Events generated by LED can be distinguished with a flag. *Daqana* also assigns an error code to the pulse shape. So good events get error code 0 and then there are some different error codes for events which causes an ADC overflow or have a double peak structure. In figure 9a a waveform which causes an ADC overflow is shown. Figure 9b shows a waveform with error code 0. The value of the baseline is also saved.

The next step is to get a calibrated spectrum. For this first the calibration coefficients has to be determined. In this step only events with error code equal to zero and the events which are not a test pulse are used. Then for every 30 minutes a histogram is made from the uncalibrated events and the calibration coefficients are determined. For this the range in which the first uncalibrated peak can be found is needed otherwise it would look for the first peak in the whole spectrum. So if the peak in the given range is found, the calibration coefficients can be calculated. If there is only one peak the coefficient is just a proportionality

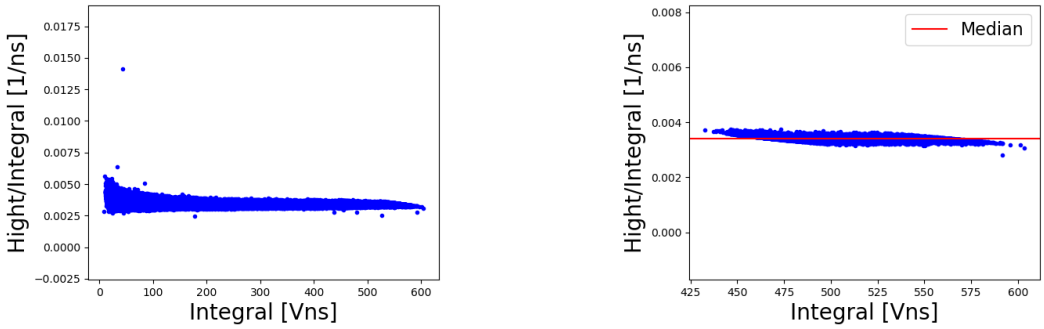

(a) (b)

Figure 10: Left: H/I scatter plot. Right: H/I scatter plot with cut at $H \geq 1.6$ and the estimated median. This is an example from Channel 1 of run_1.

constant. If there is more than one peak a first order polynomial is used. After the calibration coefficients are determined every event is then calibrated with the calibration coefficient and get an integral value corresponding to the energy. Also the corresponding data from the slow control monitor, which means all the sensor readings like temperature, humidity etc., is saved with the events.

In the last step it is iterated through all the events in one hour. All events for every channel are stored in a histogram and a fit is done for every peak. The area of the fitted peak is then taken as the rate divided by the relative time. Next to the slow control data the starting time of the measurement, the time in seconds of the bin center, the rate, the error of the rate, which channel and which peak it corresponds to, the energy of the peak and the resolution of it is saved. All these informations are needed to analyze the radioactive decay.

The data acquisition started at 18th of July 2017 and is still taking data. After almost one year the ^{54}Mn source has to be replaced because it was weak. Also the voltages on the PMTs are adjusted. To optimize the processing two representative data sets are used. One data set with the old ^{54}Mn source, which is referred to as run_1, contains 46 days of data from 18th of August 2017 to 3rd of October 2017. The second data set with the replaced source and new voltages on the PMTs is referred to as run_2. It contains 26 days of data from 12th of June 2018 to 8th of July 2018.

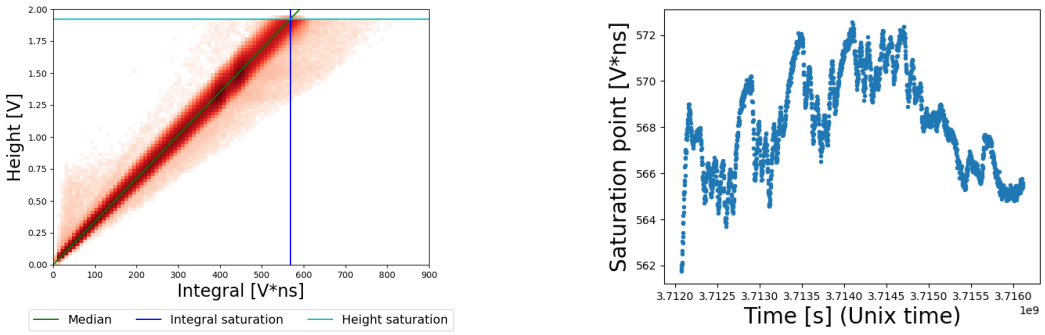

(a) (b)

Figure 11: Left: The 2D histogram of Integral vs. Height to determine the saturation point of channel 1 run_1 is shown. In the appendix A in figure A.29 and figure A.30 all histograms from run_1 and run_2 are shown. Right: The time dependency of the saturation points in channel 1 of run_1 is shown. In the appendix A in figure A.31 and figure A.32 all histograms from run_1 and run_2 can be found.

4.2. Saturation

The analog-to-digital converter (ADC) of the experiment has a $2V$ range, and every input signal is converted into 14 bit integers. If the input pulse is too high, has a difference in voltage from baseline that is larger than $2V$, then the ADC cannot fully digitize it, and the event is said to be *saturated*. An example of this is shown in figure 9a. The saturation level is given by the ADC $2V$ range minus the baseline converted into Volts: $saturation\_level = 2 - baseline \cdot 2/2^{14}$.
To know where the saturation level is, is important because the peaks in the spectra of the sources which will be analyzed should not be saturated.
The goal is to determine the saturation point in Integral and find the peaks which are not saturated. For this the intersection point of the saturation level and the median of $Height/Integral$ (H/I) is needed. As we can see in figure 10a the values with low Integral are widely scattered. This will influence the calculation of the median in just one direction. So only the data points with $H \geq 1.6$ are used to calculate the median. This we can see in figure 10b. With this the Integral saturation point can be calculated with $saturation\_point = saturation\_level/median$.
Because of some memory problems of the server these calculations have to be done for every half an hour individually. So in the end an array with saturation points is created. To calculate the values shown in figure 11a the mean of the particular values is used. However, a look is taken at the variation over time. This can be

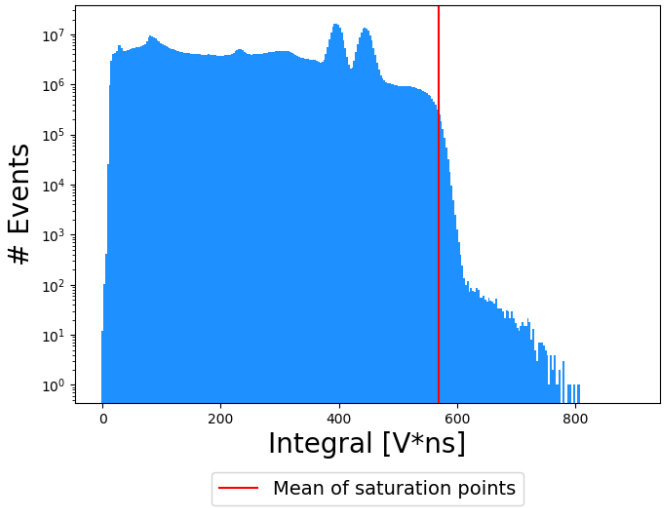

Figure 12: The integral spectrum of channel 1 in run_1 with the saturation line to find saturated peaks is shown.

seen in figure 11b where an example of channel 1 from run_1 is shown.

4.3. Peak determination

To find the peaks which are saturated first the corresponding energy of every peak has to be known. For this the uncalibrated spectra is drawn as shown in figure 12. The plots from all channels of run_1 are shown in the appendix A in figure A.33 and for run_2 in figure A.34. Also in these plots one can see the saturation line which is calculated before. To be sure that the right peaks in the spectra are used for further analysis the gain of the detector is used to determine which Integral corresponds to which energy. With the gain which is given in Vs/kev the expected energy for every integral value can be calculated by dividing the integral value with the gain. Sometimes It was hard to define which peaks are shown in the spectra. For example in figure 12 actually three peaks should be found but the trick with the gain helped to be sure that the third peak is saturated and just the first two are shown.
Peaks are selected given a range in Vns. In table 3 for every channel first the peaks in keV which can be found in a radioactive decay from the particular source and then the peaks in Vns which are found in the spectra are shown. Also the range needed for the calibration file is shown. The peaks which are saturated are marked with sat.

Source	Channel	Run	Peak 1	Range 1 [Vns]	Peak 2	Range 2 [Vns]	Peak 3	Range 3 [Vns]
			1173.2 kev		1332.5 kev		2505.7 kev	
^{60}Co	0	run_1	208 Vns	183, 222	238 Vns	222, 262	450 Vns	420, 510
		run_2	175 Vns	153, 183	199 Vns	183, 214	380 Vns	356, 420
	1	run_1	396 Vns	352, 418	448 Vns	418, 486	sat.	
		run_2	197 Vns	175, 210	224 Vns	210, 244	410 Vns	382, 448
			834.8 kev					
^{54}Mn	2	run_1	65 Vns	47, 77				
		run_2	157 Vns	129, 197				
	3	run_1	173 Vns	139, 201				
		run_2	163 Vns	133, 191				
			511 kev		1157.02 kev		1668.02 kev	
^{44}Ti	4	run_1	328 Vns	278, 384	sat.		sat.	
		run_2	131 Vns	99, 155	288 Vns	262, 320	430 Vns	388, 458
	5	run_1	450 Vns	380, 520	sat.		sat.	
		run_2	165 Vns	135, 187	366 Vns	328, 406	534 Vns	492, 578
			1460 kev					
Background	6	run_1	167 Vns	139, 181				
		run_2	113 Vns	99, 119				
	7	run_1	109 Vns	93, 123				
		run_2	121 Vns	103, 137				

Table 3: Peak energies of every channel with the peaks found in Vns and the range given to the process for the determination of the calibration coefficients. ^{60}Co has three peaks, two from the deexcitation of ^{60}Ni and the third is the sum of these if the γ-rays reach the detector at the same time, but in channel 1 only two are found. This means that the third one is saturated. ^{54}Mn only has one peak. ^{44}Ti has three but in both channel only one is shown in the spectrum. The Background channels have only one peak.

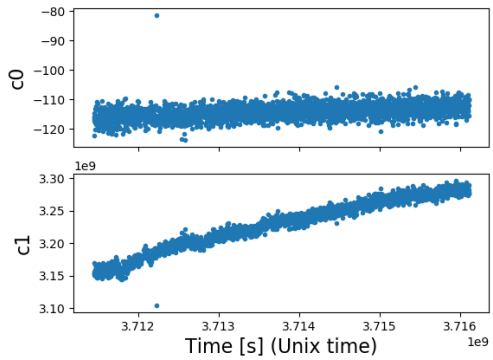

(a) Calibration coefficients over time for channel 1 in run_1. The outlier is caused from missing files in the data acquisition shown in figure 14

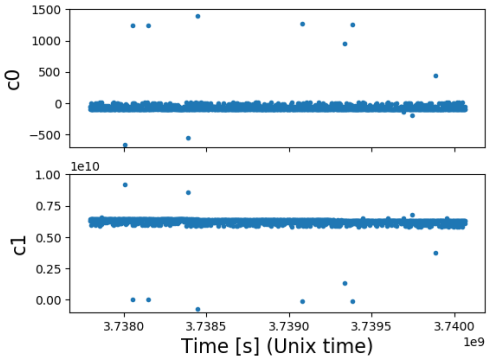

(b) Calibration coefficient over time for channel 1 in run_2. The plot shows many of outliers caused from a fitting porblem in the calibration process

Figure 13: Calibration coefficients over the time. Two examples from run_1 and run_2 with outliers. Plots from every channel can be found in the appendix A in figure A.35 for run_1 and in figure A.36 for run_2

4.4. Calibration

With the information from section 4.3 the procedure can be adjusted and the calibration can be done. Now the range of the first peak is given to the calibration procedure. In this range the maximum bin is found. To find the other peaks, if there are more than one, the fact is used that the relative distance from the peaks in the uncalibrated spectrum is the same as in the calibrated spectrum. The formula which is used to determine the integral value of the second and third peak is

$$val_n = Vs\_peak_0 \cdot \frac{E\_peak_n}{E\_peak_0} \tag{4.1}$$

where E_peak_0 is the energy of the first peak in the spectrum, E_peak_n is the energy of the peak the procedure is looking for, Vs_peak_0 is the uncalibrated integral value of the first peak and val_n is then the uncalibrated integral value in Vs of the wanted peak. Around this value a range is defined. Inside this range a Gaussian is fitted to the peak and the mean is used as the integral value of the uncalibrated peak.
To determine the calibration coefficient for a source with just one peak a simple

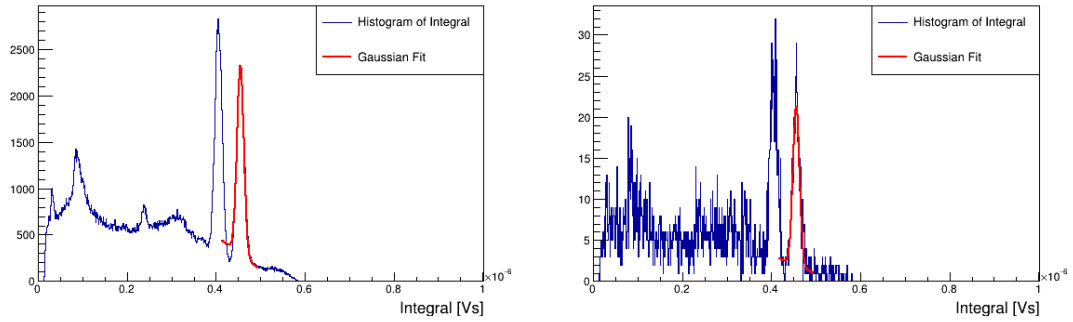

(a) (b)

Figure 14: Left: a normal spectrum with a fit for the second peak in channel 1 is shown. Right: the spectrum with the fit for the second peak which causes the outlier in the calibration coefficients is shown.

proportionality is made with c equally the calibration coefficient:

$$c = \frac{E\_peak_0}{Vs\_peak_0} \tag{4.2}$$

If there is more than one peak a 1st order polynomial $E = c_0 + c_1 \cdot I$ is used with E equals to the energy, I equals to the integral and c_0 and c_1 are the calibration coefficients. But because there is the peak energy without any error and only an appropriate error on the integral value of the peak an inverse calibration is done. This means it uses $I = v_0 + v_1 \cdot E$ as 1st order polynomial to fit the graph integral vs. energy and then just invert the function to get c_0 and c_1.

$$c_0 = -\frac{v_0}{v_1} \qquad\qquad c_1 = \frac{1}{v_1} \tag{4.3}$$

After the calibration is run, a cross check is performed. The coefficients vs. time are plotted because the calibration is done for every 1800 seconds of data. An example can be seen in figure 13. In figure 13a there is an outlier in the coefficients of channel 1. To determine why this outlier happened the spectrum with the peak fit is plotted as shown in figure 14. In 14a is a normal spectrum from channel 1 shown with a fit of the second peak. In 14b the spectrum is shown which is responsible for the outlier in channel 1. This is because there are just 3427 entries in the spectrum. After some investigation a failure in the data acquisition is found which caused some missing files. For run_1 the calibration coefficients from the other channels contain no more outliers.

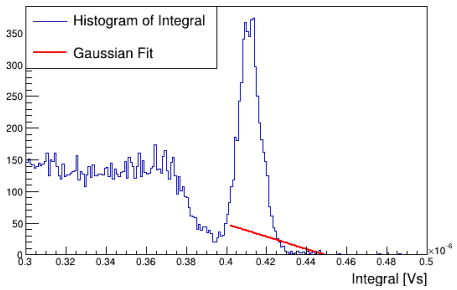

(a) Peak fit failed

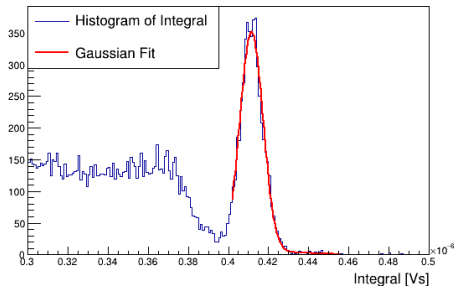

(b) Fit range is shifted to the right

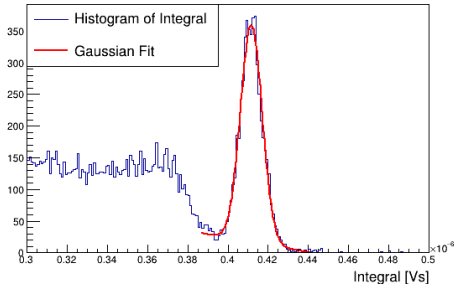

(c) Good fit

Figure 15: Spectra from the third peak fit in the calibration process for channel 1 in run_2. In (a) the fit failed. After the first improvement the peak is fitted but with a shift to the right as shown in (b). The second improvement gives a good peak fit as shown in (c)

4.4.1. Improvements on procedure

In figure 13b a large number of outliers in the distribution of the calibration coefficients can be seen. After some investigation of the calibration process it was found that these outliers were due to the failed fit as shown in figure 15a. The other peaks are fitted well only the third peak has some problems. This is due to the fitting procedure. The value of the peak is determined with a scaling of the first peak. Then a range of five sigma is defined for the fit. The problem was that the fit does not find the peak. To solve this problem the initial fit parameter is set to the actual value of the peak. This means that the highest bin in the defined range is extracted and the x-axis value of this bin is set as initial parameter.
The effect of the improvement can be seen in figure 15b. The peak is fitted but it is still shifted to the right. The fit starts left from the peak at half hight and ends on the right side far away from the peak. This causes form the fitting range which is still defined with the old peak value which was changed. In a second step the

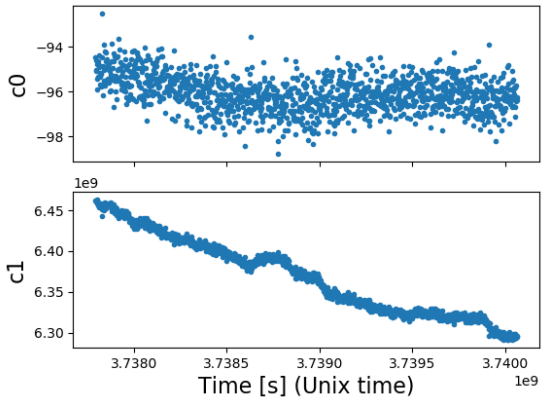

Figure 16: The calibration coefficients of channel 1 in run_2 after the changes in the calibration process. The plots from the other channels can be seen in the appendix A in figure A.37 for run_1 and in figure A.38 for run_2

fit range was also redefined. For this the same definition for the range is taken as before the first changes and they are redefined with the peak value of the highest bin.
In figure 15c the fit of the third peak of the same time stamp is shown with the second improvement. Now the fit is symmetric around the peak and the outliers in the calibration coefficient plot are gone as shown in figure 16.

Now the calibration process worked fine. The next step is the analysis of the spectra to find the decay rate.

4.5. Background corrections in analysis procedure

To find the decay rate a Gaussian is fitted to every peak in every channel. To consider the background a GEANT4 simulation is used. Both are joined and a probability density function ($p.d.f$) is constructed. The $p.d.f$ is normalized and the fraction of the contribution to the $p.d.f$ of every peak can be determined, and with these the area under the peak. The rate is obtained by dividing this area by the time interval which is defined as an hour. The error of the rate is calculated through error propagation where also the error for the background is taken into account.

After the analysis procedure the decay rates for run_1 are plotted for every channel and peak. For ^{54}Mn the rates were around 3.5 million which is really high. It was found that the fit was not working properly as shown in figure 17a. This was because the background $p.d.f$ was wrong. The reason is not known because the

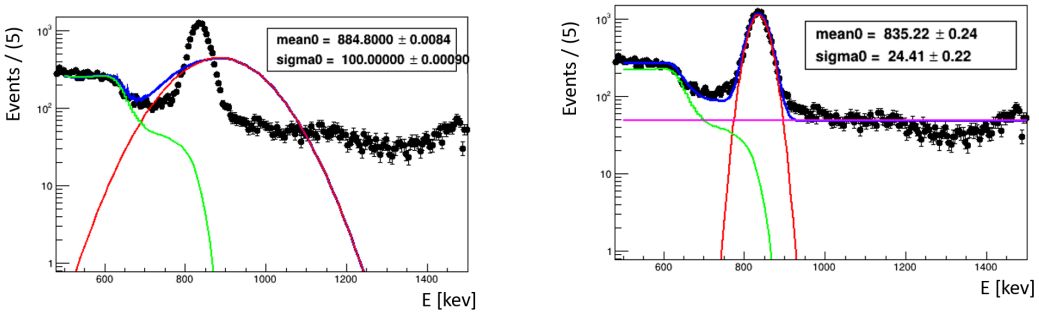

(a) (b)

Figure 17: An example from run_1 of channel 2 to show that the fit was not working on ^{54}Mn. Left: The fit of the analysis method does not work because of the background template. The peak is not fitted well. Right: The fit works well after the improvements. Instead of the simulated background template a uniform distribution is used.

procedure uses the GEANT4 simulation as background template. To make the fit working a uniform distribution is added as the background. With this change the fit works well as can be seen in figure 17b where the pink line is the uniform distribution. With this the rate is in an expected range and the data analysis can start. The analysis is described in the next section.

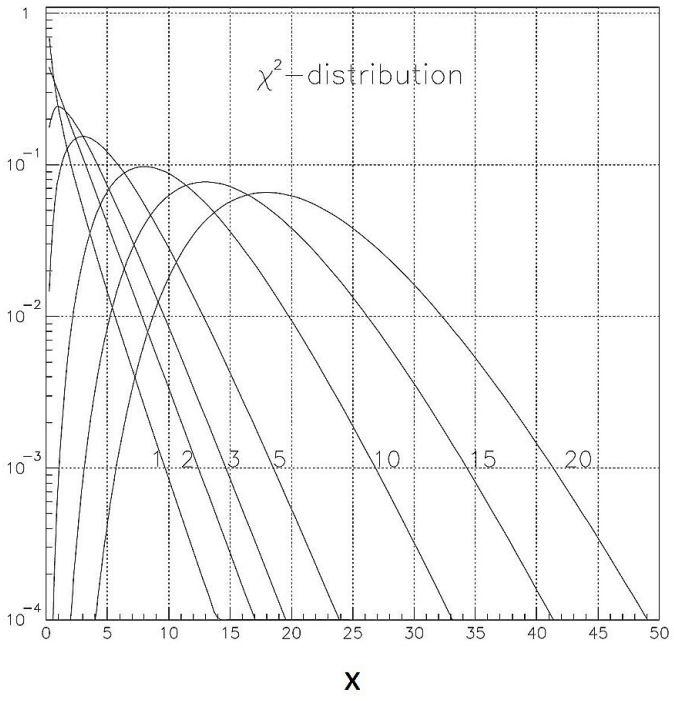

Figure 18: The shape of the χ^2 $p.d.f$ with different values of dof. [19]

5. Data Analysis

In this section the data analysis procedure is described. First a statistical framework is implemented and its cross check is described. The analysis was performed on data from 28th of July 2017 to 11th of June 2018. Unfortunately some disk space problems appeared in the data processing, hence the data after the replaced ^{54}Mn source could not be processed in an appropriate time.

5.1. Theoretical model

The radioactive decay is an exponential decay which is described by the function in equation 2.3. To check if there is a modulation in this exponential decay a modulation term is added to the exponential so that the rate can be parameterized as follows:

$$A(t) = A_0 e^{-t/\tau} \cdot (1 + \alpha \cdot \cos(\omega \cdot t - \phi)) \tag{5.1}$$

where α is the amplitude of the cosine, ω is the period of the cosine and ϕ is the phase. To fit the data with this function, the Python procedure *scipy.optimize.curve_fit*

is used. It needs as input the function, the data, the error on the data, an initial guess and also bounds can be defined for the fitted parameters. It fits the data with a least squares method which minimizes the χ^2. The χ^2 is defined as the sum of the squares of the residuals,

$$\chi^2 = \sum_{i=1}^{n} \left(\frac{y_i - f(x_i)}{\sigma_i} \right)^2 \tag{5.2}$$

where y_i are the data points, $f(x_i)$ is the fitted function, σ_i is the error on data point y_i and n is the number of data points.
The distribution of the χ^2 is fully described by one variable which is the degrees of freedom (dof). The probability density function ($p.d.f$) f_n of a χ^2 distribution with $dof = n$ is

$$f_n(x) = \frac{1}{2^{\frac{n}{2}}\Gamma(\frac{n}{2})} x^{\frac{n}{2}-1} \exp(-\frac{x}{2}). \tag{5.3}$$

The average of the distribution is equal to the dof $\mu = n$ and the variance is $Var(\chi^2) = 2n$. The shape of the distribution for different values of dof is shown in figure 18. If the $dof \to \infty$ the distribution tends to a Normal distribution. The χ^2 can be used as an indicator of the goodness of a fit [19].

5.1.1. Generate data

For a Monte-Carlo simulation data is generated as described in this section. The generated data is used to check the statistical framework and to find a limit on the amplitude α in the modulation term in a normal exponential decay.
For every monoenergetic line in the data which will be analyzed 1000 data sets are generated with initial decay rate, A, set to the value of the very first entry in the data acquisition of the modulation experiment. In table 4 the values for the function

$$f(t) = A \cdot e^{-t/\tau} \tag{5.4}$$

are shown. The values are chosen while taking into account the gaps in the data acquisition if a run was stopped and the next one started a few hours later. In channel 3 the high voltage supplier tripped for some hours. This gap is also taken into account and is modeled in the simulation data.
With these values data is generated with the exponential decay function 5.4. Because the rates are given in bins of an hour, to calculate every value of the data set the integral $I = (f(a_n) + f(a_{n+1}))/2$ is taken where a_n are the bin edges. The

Channel	Peak [keV]	A	τ	# Bins
0	1173.2	27.73317	5.27 y	7542
	1332.5	23.96626	5.27 y	7542
1	1173.2	29.75619	5.27 y	7542
	1332.5	26.58419	5.27 y	7542
2	834.8	3.906610	312.2 d	7542
3	834.8	4.462543	312.2 d	7485
4	511.00	194.6683	59.1 y	7542
5	511.00	169.9193	59.1 y	7542

Table 4: Initial parameters for the Monte-Carlo simulation. A is given per second and the number of bins are distributed over the data taking time of 7633 hours. This means that the gaps in the data acquisition are simulated. In channel 3 the high voltage supply tripped and caused a larger gap in the data acquisition which is taken into account too.

error in I is the square root of it $e_I = \sqrt{I}$. A Poisson distribution is equal to a Gaussian for large sample size. So to randomize the entries a random number from a Gaussian with mean $\mu = I$ and a standard deviation $\sigma = e_I$ is extracted. This random value r is now the entry for the particular bin and the error on it is again the square root of it $e_r = \sqrt{r}$. While doing this process the gaps of the data acquisition are simulated at the same time as found in the data.
Datasets generated in this way are referred to in the following as ds_0.

5.1.2. Cross checks on fitting algorithm

The statistical properties of the fitting algorithm are tested on the generated ds_0 datasets by fitting them with the function in equation 5.4. The values of the fitted parameter are expected to be distributed as a Gaussian around the true value. Also the χ^2 of the fits are determined and compared with the expected distribution. In figure 19 the fitting result is shown from the 1173.2 keV peak of channel 1. In figure 19a the $p.d.f$ of the calculated χ^2 is shown compared with the theoretical one. In the figures 19b and 19c the Gaussian distribution of the two parameters A and τ around the *true* value of ds_0 can be seen.
In addition to this a "check" data set ds_{check} is generated with 1000 sets of radioactive decay. It is generated with the function in equation 5.1 with $\alpha = 0.2$ and $\phi = 1.5\pi$. This data set is fitted with the same function it was generated and the parameter distribution is shown in figure 20 where an example of the 1173.2 keV peak from channel 1 is shown.

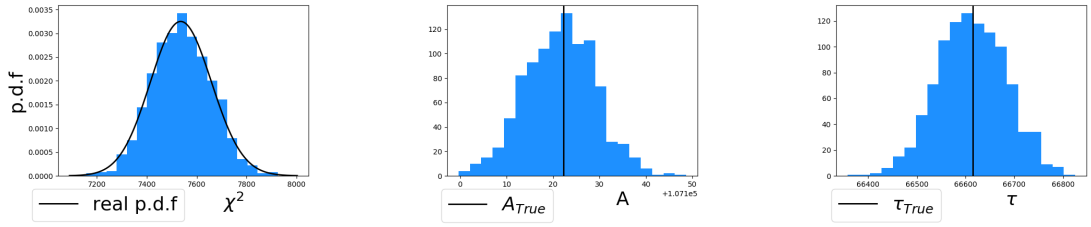

(a) (b) (c)

Figure 19: An example of the fitting results of ds_0 with an exponential function from the 1173.2 keV peak of channel 1. (a) is the chi^2 distribution, (b) the histogram of the fitted parameter A and (c) the histogram of the fitted parameter τ. The other plots can be seen in the appendix A in figure A.39.

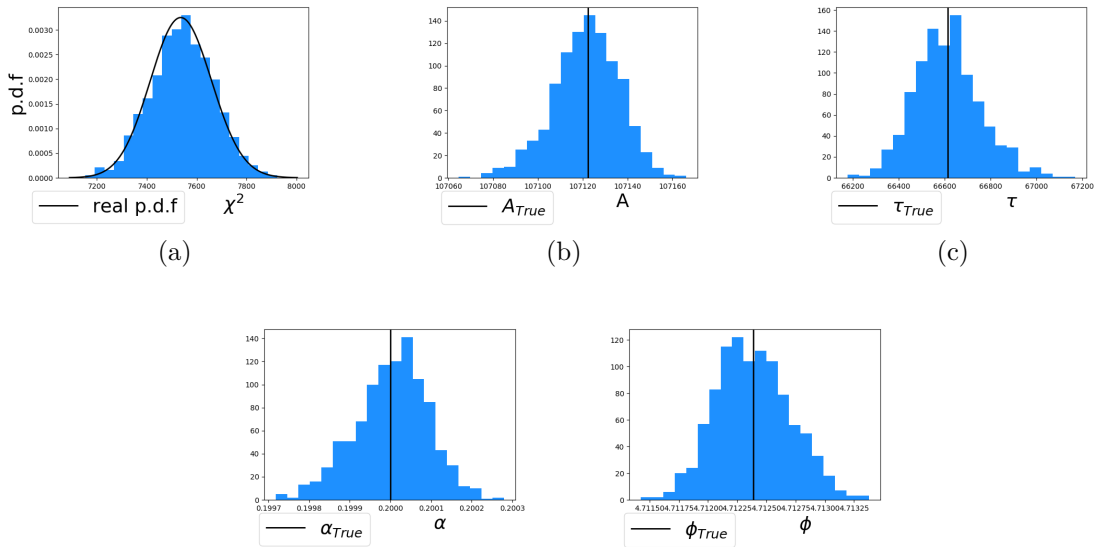

(a) (b) (c)

(d) (e)

Figure 20: An example of the fitting results of ds_{check} with the modulation function of equation 5.1 from the 1173.2 keV peak of channel 1. The histograms of the fitted parameters (a) chi^2 distribution, (b) A, (c) τ, (d) α and (e) ϕ are shown. The other plots can be seen in the appendix A in figure A.40.

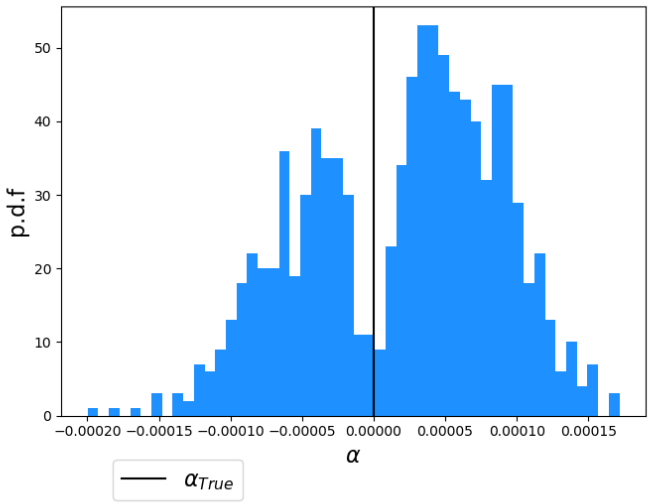

Figure 21: Double peak structure in channel 4 while fitting the modulation function to ds_0.

Channel	Peak [keV]	Bias
0	1173.2	$8.9 \cdot 10^{-5}$
	1332.5	$9.0 \cdot 10^{-5}$
1	1173.2	$8.5 \cdot 10^{-5}$
	1332.5	$8.6 \cdot 10^{-5}$
2	834.8	$2.8 \cdot 10^{-4}$
3	834.8	$2.5 \cdot 10^{-4}$
4	511.00	$3.3 \cdot 10^{-5}$
5	511.00	$3.4 \cdot 10^{-5}$

Table 5: The bias is the mean of the histogram of α if ds_0 is fitted with the modulation function

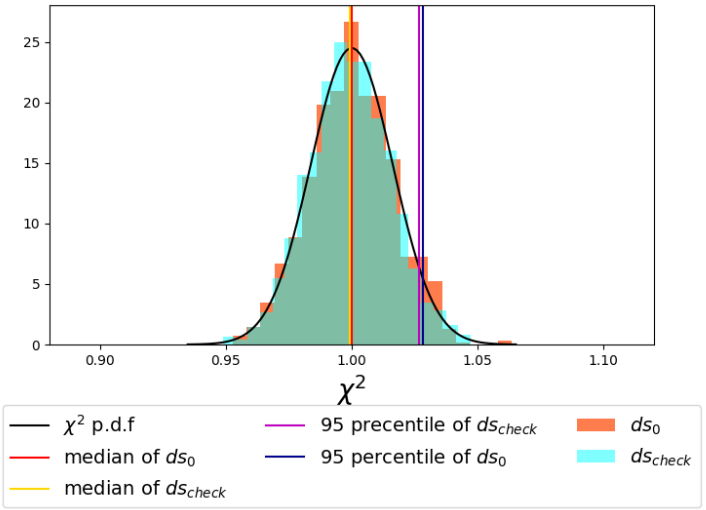

Figure 22: Reduced χ^2 distributions of the fit of ds_0 and ds_{check} with $\alpha_{true} = \alpha_{fit}$. Also the 95 percentile and the median is shown to compare both distributions. This example is from channel 4. The other plots are shown in the appendix A in figure A.41

In the vast majority of eases the fitting algorithm was found to perform well. But a small problem was found when fitting ds_0 with the modulation function:

$$A(t) = A_0 e^{-t/\tau} \cdot (1 + \alpha \cdot \cos(\omega \cdot t - \phi)) \tag{5.5}$$

The fitted α is expected to be most likely 0 because the data set is constructed with a normal exponential decay.
However, if the modulation function of equation 5.5 is fitted to the data set ds_0 a double peak structure is given for α as shown in figure 21 for the 511.00 keV peak of channel 4. Also fitting ds_0 with other initial guesses or constraints gave no better results. The problem is that this shift will bias the limit on α. For the analysis α is constrained to be positive. The shift on α from zero while fitting ds_0 with the modulation function is summarized in table 5.

5.2. Statistical inference

The goal is to test for annual modulation. In case a modulation is not found, an exclusion limit will be set on the modulation parameter α. To compute exclusion limit we use the χ^2 of the fit as a test statistic. A hypothesis α is considered

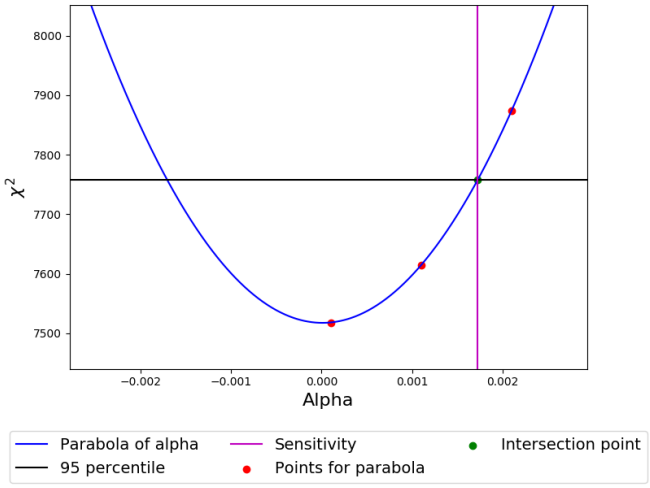

Figure 23: The parabolic shape of the χ^2 as a function of α. The parabola function is determined with the three marked points. The sensitivity is then the intersection point of the parabola and the χ^2 at the 5% $P - value$. This is one example of sensitivity estimation of the 1173.2 keV peak from channel 0.

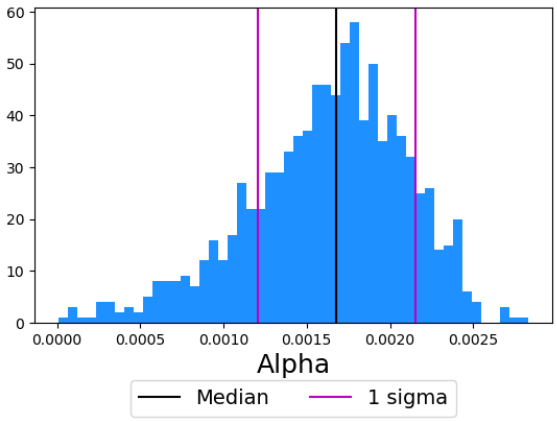

Figure 24: Histogram of the α values which causes a χ^2 which corresponds to the $P - value$. The standard deviation which is used as statistical error is marked with a magenta colored line. This is an example of the 1173.2 keV peak in channel 0. The plots for the other channels and peaks are shown in the appendix A in figure A.42

excluded at 95% confidence level if the $P-value$ is 5%. The $P-value$ gives the probability that the obtained result is compatible with the observation while the null-hypothesis is true [19]. The underlying assumption is that any modulation hypothesis with parameter α, if true, will lead to a perfect χ^2 distribution for the test-statistic used.

The first step, is to show that for data sets with a modulation amplitude of a particular α the χ^2 distribution is exactly the same as the χ^2 distribution of ds_0. For this the data set ds_{check} is taken and fitted with the modulation function. But this time $\alpha_{true} = \alpha_{fit}$ is set. This means α is fixed to its true value and just fit the other parameters. The χ^2 distributions of both fitted data sets are shown in figure 22.
The shown median and $P-value$ are equal and so the assumption that for every α value the χ^2 distributions are the same is made.

The procedure used to set a limit on α is the following:
One needs to find the value of α for which the χ^2 computed for the dataset and α has a $P-value$ of 5%. The data set ds_0 is fitted with the modulation function, but α is fixed to a particular value and the corresponding χ^2 is estimated. Because the χ^2 as a function of α has a parabolic shape only three different α values have to be fitted. With three points the parabola function $f(x) = ax^2 + bx + c$ can be reconstructed. With this function the intersection point of it with the χ^2 value which corresponds to the 5% quantile needs to be found. This is shown in figure 23. After doing this for all the 1000 data sets the histogram is made and the median is taken as sensitivity. An example of such a histogram is shown in figure 24. All sensitivity values are shown in table 6. The bias which is described in section 5.1.2 is taken into account and added as a systematic error on the sensitivity.

To cross check the results a data set ds_{sens} is generated with a modulation amplitude which is equals the estimated sensitivity. If ds_{sens} is fitted with only an exponential function the median of its χ^2 distribution should be equal to the 5% $P-value$ of the χ^2 distribution of ds_0. As can be seen in figure 25 the median of the χ^2 distribution of ds_{sens} is a bit (<2%) off. Due to the fact that one can obtain a low $P-value$ independently from α, the null hypothesis can be excluded, a correction can be applied by subtracting the best fit χ^2 to the test-statistic. The method used is simpler and conservative.

Channel	Peak [keV]	Sensitivity
0	1173.2	$(1.7 \pm 0.5^{STAT} \pm 0.1^{SYS}) \cdot 10^{-3}$
	1332.5	$(1.7 \pm 0.5^{STAT} \pm 0.1^{SYS}) \cdot 10^{-3}$
1	1173.2	$(1.5 \pm 0.5^{STAT} \pm 0.1^{SYS}) \cdot 10^{-3}$
	1332.5	$(1.6 \pm 0.5^{STAT} \pm 0.1^{SYS}) \cdot 10^{-3}$
2	834.8	$(5.1 \pm 1.5^{STAT} \pm 0.3^{SYS}) \cdot 10^{-3}$
3	834.8	$(4.8 \pm 1.4^{STAT} \pm 0.3^{SYS}) \cdot 10^{-3}$
4	511.00	$(6.0 \pm 1.7^{STAT} \pm 0.3^{SYS}) \cdot 10^{-4}$
5	511.00	$(6.1 \pm 1.8^{STAT} \pm 0.3^{SYS}) \cdot 10^{-4}$

Table 6: The sensitivity of every peak in every channel with its statistical and systematic error.

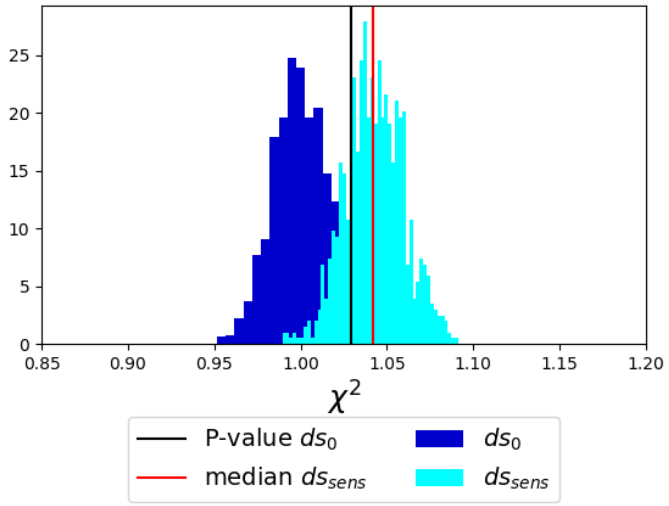

Figure 25: The χ^2 distribution of ds_0 and ds_{sens} are compared. The median of ds_{sens} should be equal to the $P - value$ of ds_0. But it is a bit shifted (<2%) to the right. This is an example from the 1173.2 keV peak of channel 0. The other plots can be seen in the appendix A in figure A.43

Channel	Peak [keV]	Half-life	Theoretical half-life	Ref.
0	1173.2	5.31(1) y	5.271(4) y	[16]
	1332.5	5.31(1) y		
1	1173.2	5.30(1) y		
	1332.5	5.26(1) y		
2	834.8	325.7(3) d	312.2(2) d	[15]
3	834.8	322.0(2) d		
4	511.00	64.7(5) y	59.1(3) y	[14]
5	511.00	61.9(5) y		

Table 7: Half-life of the measured decay rates compared to the theoretical value.

5.3. Finding the modulation limit

With all the statistical background and the improved processing the analysis of the data, before the replaced ^{54}Mn source, is possible. The data is taken from 28.07.2017 to 11.06.2018, thus almost one year. Figure 26 shows the data rate (for all the channels) as a function of time. Due to detector instability and processing artefacts, some of these data present clear non-physical values. Selection criteria are applied to the data to remove those events. These selection are defined as follows:
The first step was that if the rate is smaller than 0.2 events per second it is cut off. If a rate is so small there has to be something wrong with the measurement. For example, as mentioned before, the tripped high voltage supply in channel 3. These points are marked with green in the plots of figure 26.
For the next step a function was fitted to the data and the difference of the data points and the function is taken and divided by the error of the data points. With these quantities a histogram is made and a Gaussian is fitted to it. Every data point which is more far away than the mean $\mu \pm 3.5\sigma$ is marked as outlier. In the plots of figure 26 they are marked in red.
In the last step a cut is made due to the size of the error. There are some rates with a really large error bar which is ten times higher than the one from the others. So a histogram of all errors is made and a cut is performed where the gap of these values are. These points are marked with black in the plots of figure 26.

After all the outliers are removed as shown in figure 27 the half-life is fitted and compared with the theoretical values. For this the exponential function of equation 5.4 is fitted to the data. Because the temperature systematically influences the experimental setup most, the data is corrected with the temperature difference

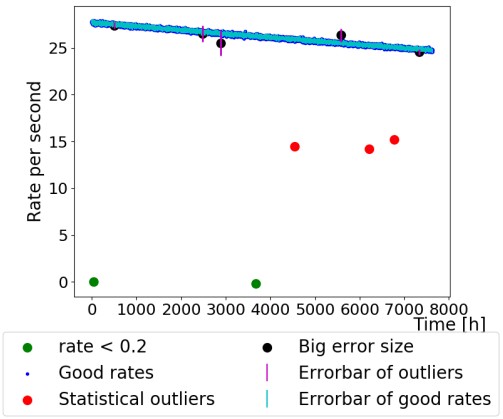

(a) Channel 0 peak 1173.2 keV

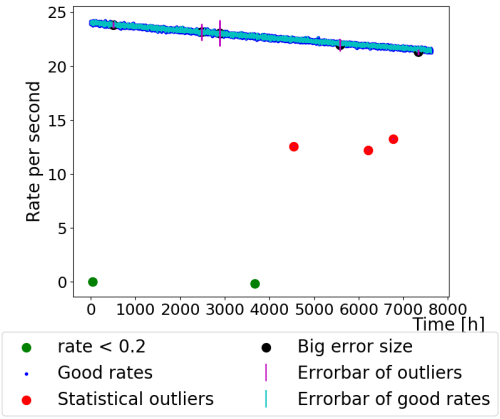

(b) Channel 0 peak 1332.5 keV

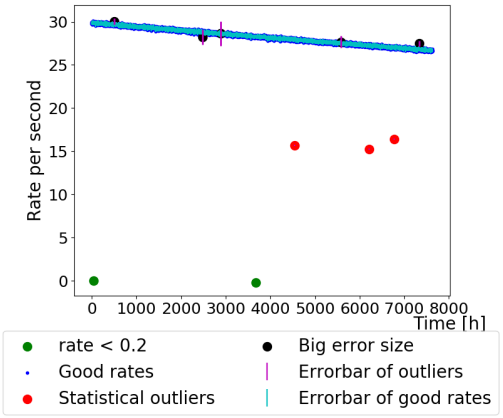

(c) Channel 1 peak 1173.2 keV

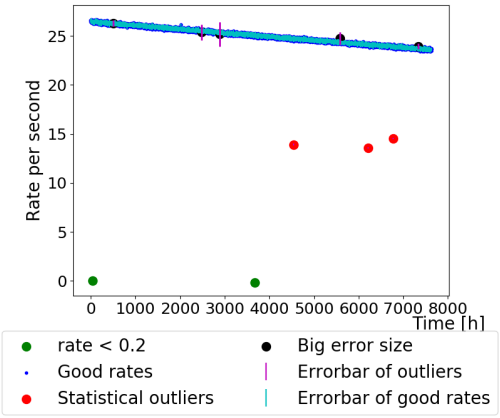

(d) Channel 1 peak 1332.5 keV

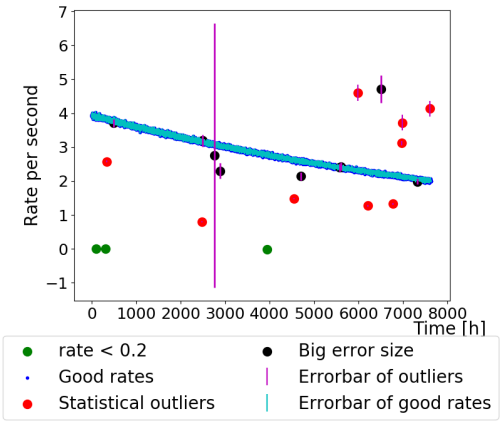

(e) Channel 2 peak 834.8 keV

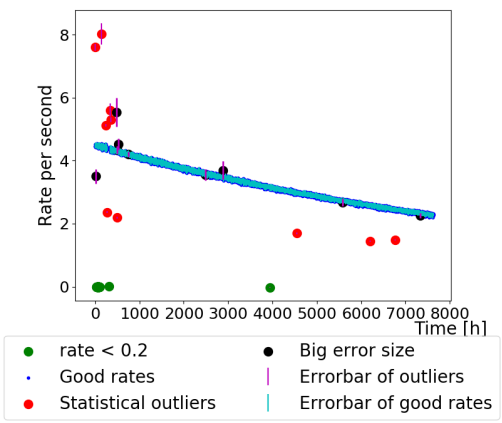

(f) Channel 3 peak 834.8 keV

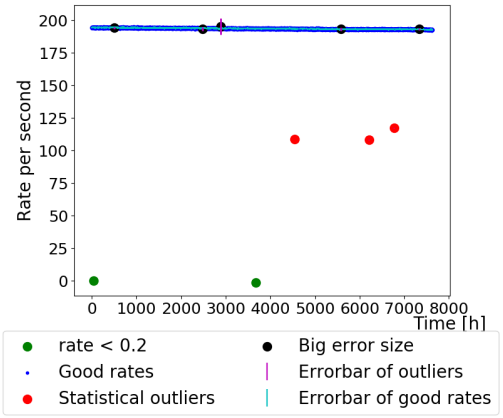

(g) Channel 4 peak 511.00 keV

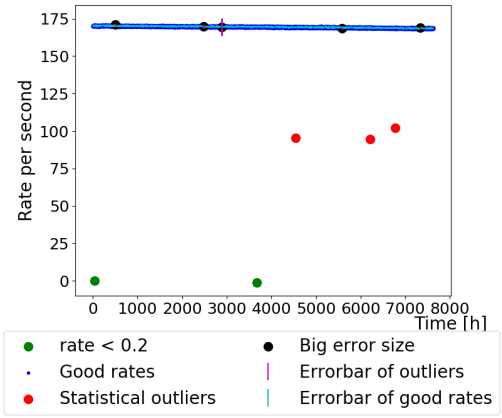

(h) Channel 5 peak 511.00 keV

Figure 26: For every channel and peak, the outliers are cut off in three steps. The first is that all rates < 0.2 are cut and marked with green points. Then all rates where the difference of the function and the point divided by the error is outside of a 3.5σ confidence interval are marked with red and are cut off. The last step is to remove all points with an error which is obviously much higher than it should be. These points are marked with black.

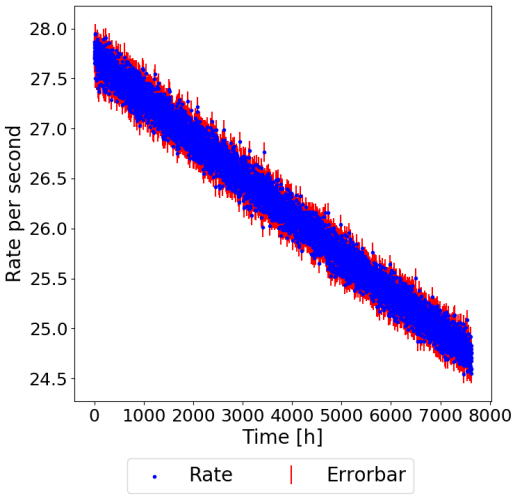

Figure 27: The rate in seconds with error bar for the 1173.2 keV peak of channel 0. The plots for the other peaks and channels can be found in the appendix A in figure A.44

from the median of the monitored temperature. So the function used has an additional term with the temperature difference.

$$f(t) = A_0 \cdot e^{-t/\tau} \cdot (1 + \beta \Delta T) \tag{5.6}$$

Only the temperature deviation of the mean temperature is interesting not the actual temperature. The data is fitted with the function of equation 5.6 and the half-life of the different peaks and channels is calculated. The results are summarized in table 7. The half-life of ^{60}Co are the best results. The half-lives of ^{54}Mn and ^{44}Ti are incompatible with the theoretical value. This is on one side due to the fact that only data for almost one year is fitted. This is a really short time to determine the exactly half-life of ^{44}Ti. On the other side the ^{54}Mn source was produced in 2013 and with its small half-life it had a really small activity at the measuring time and thus the source was weak. Because of this it was replaced on 11th of June 2018.

Despite the unsatisfying results for the half-lives, the limits on the amplitude α are still determined. To find a limit the same procedure as already performed for the simulation which was discussed in section 5.2 is applied. The data is fitted with the function

Channel	Peak [keV]	Sensitivity	Alpha limit
0	1173.2	$(1.7 \pm 0.5^{STAT} \pm 0.1^{SYS}) \cdot 10^{-3}$	$1.3 \cdot 10^{-3}$
	1332.5	$(1.7 \pm 0.5^{STAT} \pm 0.1^{SYS}) \cdot 10^{-3}$	$2.0 \cdot 10^{-3}$
1	1173.2	$(1.5 \pm 0.5^{STAT} \pm 0.1^{SYS}) \cdot 10^{-3}$	$2.0 \cdot 10^{-3}$
	1332.5	$(1.6 \pm 0.5^{STAT} \pm 0.1^{SYS}) \cdot 10^{-3}$	$2.7 \cdot 10^{-3}$
2	834.8	$(5.1 \pm 1.5^{STAT} \pm 0.3^{SYS}) \cdot 10^{-3}$	$5.3 \cdot 10^{-3}$
3	834.8	$(4.8 \pm 1.4^{STAT} \pm 0.3^{SYS}) \cdot 10^{-3}$	$5.3 \cdot 10^{-3}$
4	511.00	$(6.0 \pm 1.7^{STAT} \pm 0.3^{SYS}) \cdot 10^{-4}$	NAN
5	511.00	$(6.1 \pm 1.8^{STAT} \pm 0.3^{SYS}) \cdot 10^{-4}$	$7.7 \cdot 10^{-4}$

Table 8: The sensitivity found with the Monte-Carlo simulation in section 5.2 is compared with the limits on α found in the data.

$$f(t) = A_0 \cdot e^{-t/\tau} \cdot (1 + \beta \Delta T) \cdot (1 + \alpha \cdot \cos(\omega \cdot t - \phi)) \tag{5.7}$$

where again the data is corrected with the temperature and ω is fixed to one year because we are interested in yearly modulation. The results are summarized in table 8. The sensitivity which was calculated with the Monte-Carlo simulation in section 5.2 and the limits of α found in the data are both shown. In channel 4 the parabola of α had no intersection point with the χ^2 of the corresponding $P - value$. This means that even the null hypothesis is excluded, this has to be investigated further.

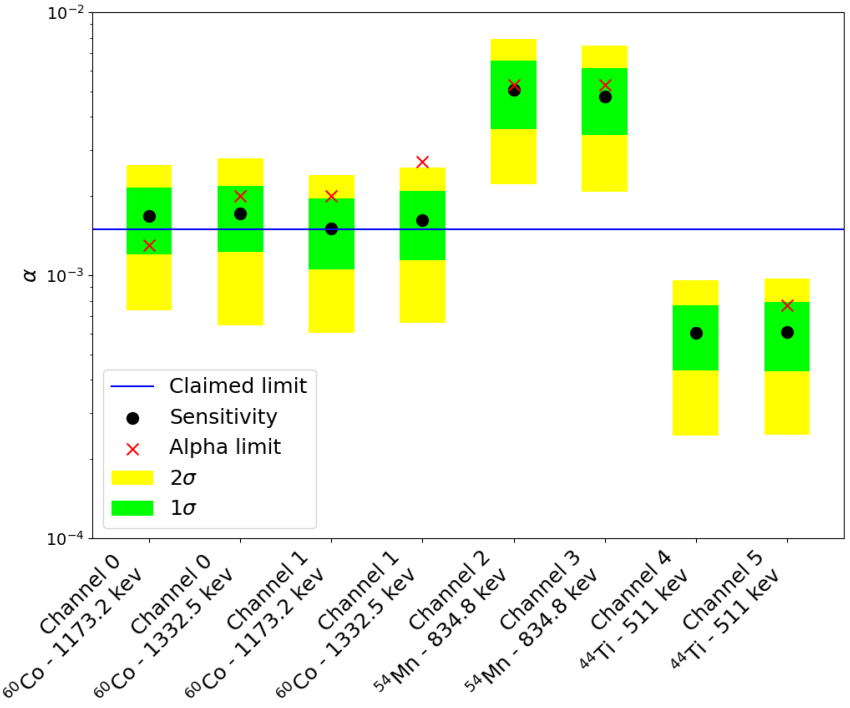

Figure 28: The sensitivity shows the expected median amplitude in a data set with no modulation and is marked with a black dot. With green the 1σ and with yellow the 2σ standard deviation of the sensitivity is marked. The blue line is the claimed modulation amplitude from Jenkins et al. [2]. The red crosses show the estimated α-limits in the data of the Zurich detectors. In channel 4 no limit could be estimated.

6. Results

In figure 28 the sensitivity, the limit on α for the data set and the claimed modulation amplitude value by Jenkins et al. [2] are shown. The limits on most of the channels are consistent with the expectation, with the exception of the ^{60}Co line at 1332.5 keV, where a 2σ excess is seen.
The sensitivity of the ^{60}Co source is around the claimed value by Jenkins et al. [2]. If the data set after the replaced ^{54}Mn source will be included in the analysis the sensitivity is expected to decrease, and a better comparison can be made.
Channel 2 and 3 have similar results. The limit on α is very consistent with the sensitivity even if the sensitivity is above the claimed modulation amplitude

of Jenkins et al. [2]. The replaced ^{54}Mn source should give better results for comparison.
For channel 4 no α limit is shown because fitting the data with the modulation function causes no result with an χ^2 which lies inside the 95% confidence level of the χ^2 $p.d.f$. This means that even the null-hypothesis is excluded, thus more investigation on the model for this channel are needed. In channel 5 the limit on α is consistent with the expected amplitude. The sensitivity and limit on α is below the claimed modulation by Jenkins et al. [2] and is of order $\mathcal{O}(10^{-4})$.

If the data after the replaced ^{54}Mn source would be included the half-life fits are expected to be more consistent with the theory values. Also the sensitivity is expected to decrease and lie below the claimed amplitude by Jenkins et al. [2]. Then the found limits on α in the data can be compared with the claimed value.

7. Conclusion

Radioactive decay is a widely assumed to be a spontaneously process which is not influenced by external conditions. However, in recent years claims of an annual modulation in long-lived isotopes are made by Jenkins et al. [2]. The modulation experiment is constructed to re-examine the idea of annual modulation and investigate the stability of decay rates with time. The experiment contains four setups located on three different continents to examine seasonal influences.

In this thesis a full data analysis of the modulation experiment is presented. To achieve this, several problems were solved during this work. For example, the background simulation of the ^{54}Mn source was not working in the analyzer file. The solution was to construct a uniform distribution which was used as background. This solution is not based on a physical meaning. It was done because it would have been too time consuming to either redo the Monte-Carlo simulation or to model a background distribution from the background detectors.
Another problem was the disk space and the long time the data processing needed. Because of this only almost one year of data could be analyzed which is not enough to get consistent results of the half-life for the ^{54}Mn and ^{44}Ti isotopes. However, the result of the found limit on the modulation amplitude α is comparable with the sensitivity found by a Monte-Carlo simulation.

In the data analysis the statistical framework was simplified to an appropriate level. With a more precise statistical analysis the result will might be more consistent with the theory. Also the LED can be included in the analysis to study the efficiency of the whole measurement.

The next step on the modulation experiment is to combine the results of the different detector locations. In a first step, which already started, the data from the Zurich detectors and Nikhef are combined and a statistical combination of the result will be performed.

List of Figures

List of Tables

References

[1] Jörn Bleck-Neuhaus. *Elementare Teilchen*. Springer-Lehrbuch. Springer Berlin Heidelberg, Berlin, Heidelberg, 2010. ISBN 978-3-540-85299-5. doi:10.1007/978-3-540-85300-8.

[2] Jere H. Jenkins, Ephraim Fischbach, John B. Buncher, John T. Gruenwald, Dennis E. Krause, and Joshua J. Mattes. Evidence of correlations between nuclear decay rates and Earth–Sun distance. *Astroparticle Physics*, 32(1): 42–46, aug 2009. ISSN 09276505. doi:10.1016/j.astropartphys.2009.05.004.

[3] E. N. Alexeyev, Yu. M. Gavrilyuk, A. M. Gangapshev, V. V. Kazalov, V. V. Kuzminov, S. I. Panasenko, and S. S. Ratkevich. Results of a search for daily and annual variations of the Po-214 half-life at the two year observation period. may 2015. doi:10.1134/S1063779616060034.

[4] A. G. Parkhomov. Researches of alpha and beta radioactivity at long-term observations. apr 2010. URL `http://arxiv.org/abs/1004.1761`.

[5] Eric B. Norman, Edgardo Browne, Howard A. Shugart, Tenzing H. Joshi, and Richard B. Firestone. Evidence against correlations between nuclear decay rates and Earth–Sun distance. *Astroparticle Physics*, 31(2):135–137, mar 2009. ISSN 09276505. doi:10.1016/j.astropartphys.2008.12.004.

[6] E. Bellotti, C. Broggini, G. Di Carlo, M. Laubenstein, R. Menegazzo, and M. Pietroni. Search for time modulations in the decay rate of 40k and 232th. *Astroparticle Physics*, 61:82 – 87, 2015. ISSN 0927-6505. doi:10.1016/j.astropartphys.2014.05.006.

[7] E. Bellotti, C. Broggini, G. Di Carlo, M. Laubenstein, and R. Menegazzo. Search for time dependence of the 137Cs decay constant. *Physics Letters B*, 710(1):114–117, mar 2012. ISSN 03702693. doi:10.1016/j.physletb.2012.02.083.

[8] Wolfgang Demtröder. *Experimentalphysik 4*. Springer-Lehrbuch. Springer Berlin Heidelberg, Berlin, Heidelberg, 2017. ISBN 978-3-662-52883-9. doi:10.1007/978-3-662-52884-6.

[9] Bogdan Povh, Klaus Rith, Christoph Scholz, Frank Zetsche, and Werner Rodejohann. *Teilchen und Kerne*. Springer-Lehrbuch. Springer Berlin Heidelberg, Berlin, Heidelberg, 2014. ISBN 978-3-642-37821-8. doi:10.1007/978-3-642-37822-5.

[10] Glenn F Knoll. *Radiation detection and measurement*. Wiley, Hoboken, N.J, 4th ed. edition, 2010. ISBN 978-0-470-13148-0.

[11] Claus Grupen and Boris Shwartz. *Particle Detectors*. Cambridge Monographs on Particle Physics, Nuclear Physics and Cosmology. Cambridge University Press, Cambridge, 2 edition, 2008. ISBN 9780511534966. doi:10.1017/CBO9780511534966.

[12] D.E. Alburger, G. Harbottle, and E.F. Norton. Half-life of32si. *Earth and Planetary Science Letters*, 78(2):168 – 176, 1986. ISSN 0012-821X. doi:10.1016/0012-821X(86)90058-0.

[13] J. R. Angevaare, P. Barrow, L. Baudis, P. A. Breur, A. Brown, A. P. Colijn, G. Cox, M. Gienal, F. Gjaltema, A. Helmling-Cornell, M. Jones, A. Kish, M. Kurz, T. Kubley, R. F. Lang, A. Massafferri, R. Perci, C. Reuter, D. Schenk, M. Schumann, and S. Towers. A Precision Experiment to Investigate Long-Lived Radioactive Decays. *Journal of Instrumentation*, 13 (07):P07011–P07011, apr 2018. ISSN 1748-0221. doi:10.1088/1748-0221/13/07/P07011.

[14] Jun Chen, Balraj Singh, and John A. Cameron. Nuclear Data Sheets for A = 44. *Nuclear Data Sheets*, 112(9):2357–2495, sep 2011. ISSN 00903752. doi:10.1016/j.nds.2011.08.005.

[15] Huo Junde and Huo Su. Nuclear Data Sheets for A = 54. *Nuclear Data Sheets*, 107(6):1393–1530, jun 2006. ISSN 00903752. doi:10.1016/j.nds.2006.05.003.

[16] J.K. Tuli. Nuclear Data Sheets for A = 60. *Nuclear Data Sheets*, 100(3): 347–481, nov 2003. ISSN 00903752. doi:10.1006/ndsh.2003.0017.

[17] E. Browne and J.K. Tuli. Nuclear Data Sheets for A = 137. *Nuclear Data Sheets*, 108(10):2173–2318, oct 2007. ISSN 00903752. doi:10.1016/j.nds.2007.09.002.

[18] Hermann Kolanoski and Norbert Wermes. *Teilchendetektoren*. Springer Berlin Heidelberg, Berlin, Heidelberg, 2016. ISBN 978-3-662-45349-0. doi:10.1007/978-3-662-45350-6.

[19] T. Del Prete. Methods of Statistical Data Analysis in High Energy Physics. Technical report, Instituto Nazionale di Fisica Nucleare, Pisa, 2000. URL `www.pg.infn.it/l3/biasini/dott/delprete.ps`.

A. Figures

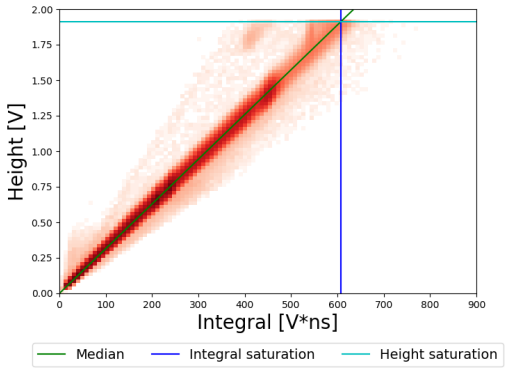

(a) Channel 0

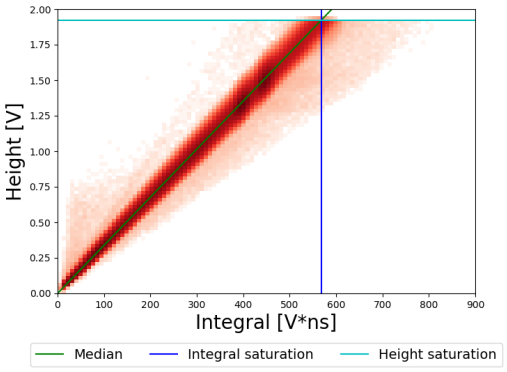

(b) Channel 1

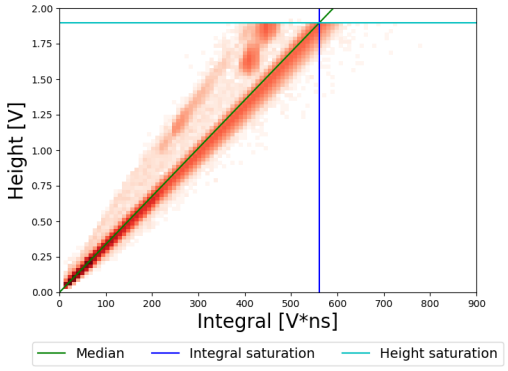

(c) Channel 2

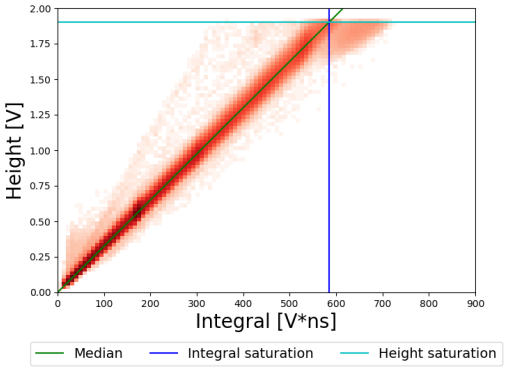

(d) Channel 3

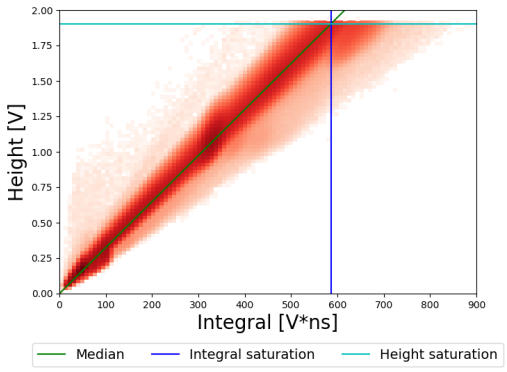

(e) Channel 4

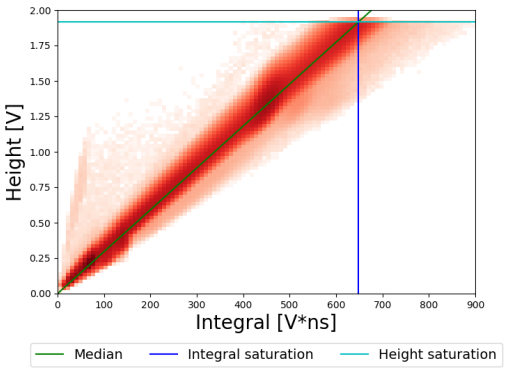

(f) Channel 5

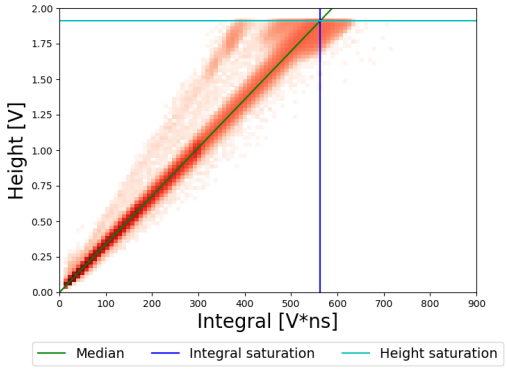

(g) Channel 6

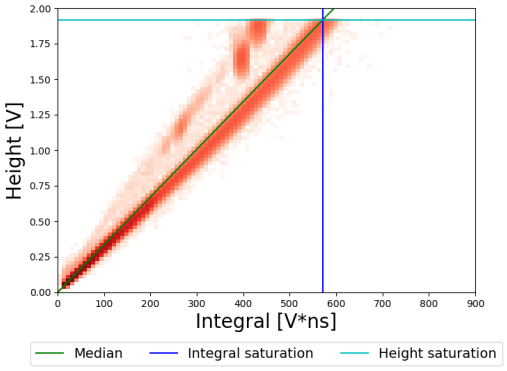

(h) Channel 7

Figure A.29: 2D Histogram of all channels with the saturation level, the integral saturation point and the median of run_1

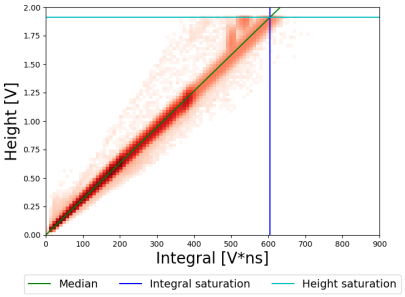

(a) Channel 0

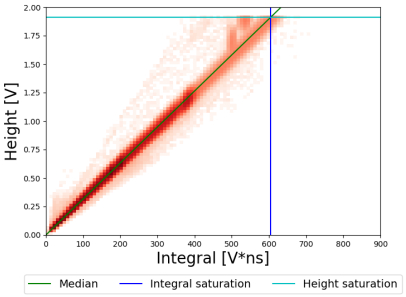

(b) Channel 1

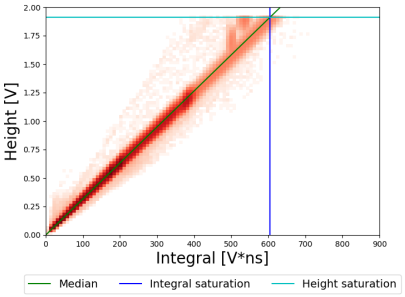

(c) Channel 2

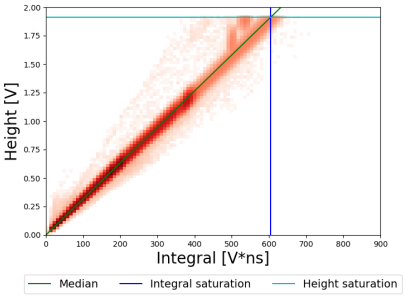

(d) Channel 3

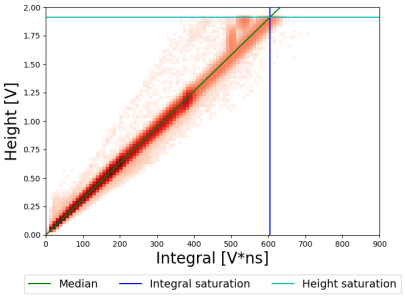

(e) Channel 4

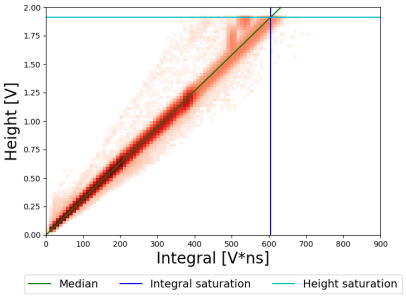

(f) Channel 5

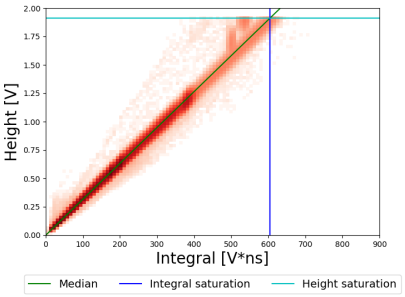

(g) Channel 6

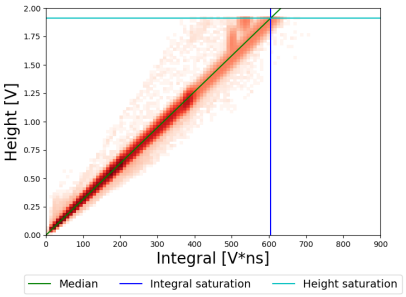

(h) Channel 7

Figure A.30: 2D Histogram of all channels with the saturation level, the integral saturation point and the median of run_2

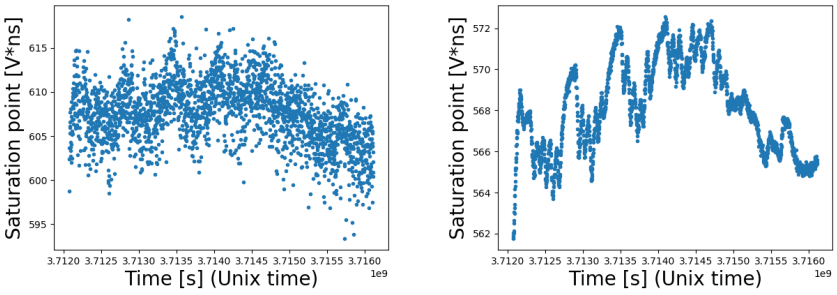

(a) Channel 0

(b) Channel 1

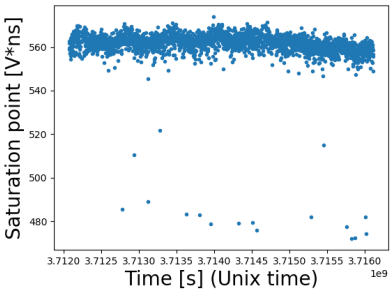

(c) Channel 2

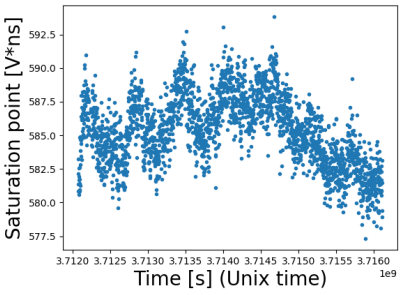

(d) Channel 3

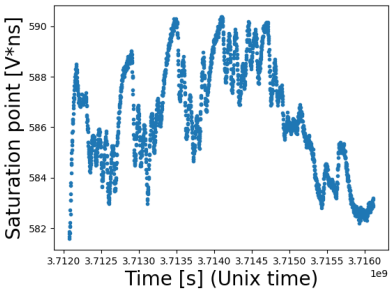

(e) Channel 4

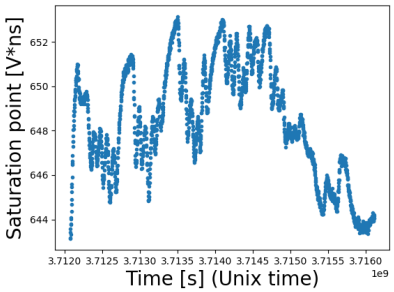

(f) Channel 5

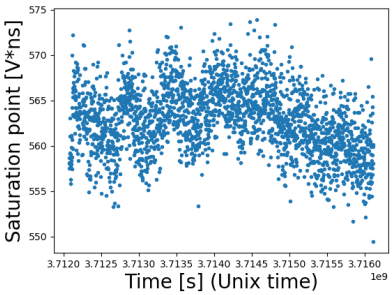

(g) Channel 6

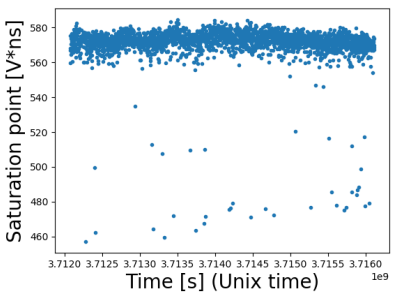

(h) Channel 7

Figure A.31: Variation of the saturation points over the time for run_1

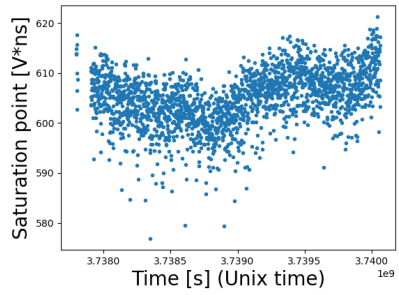

(a) Channel 0

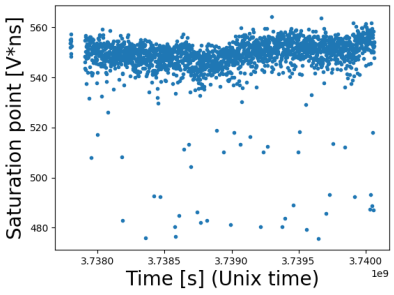

(b) Channel 1

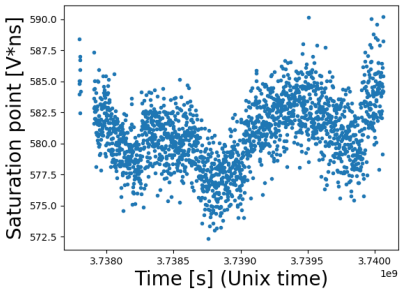

(c) Channel 2

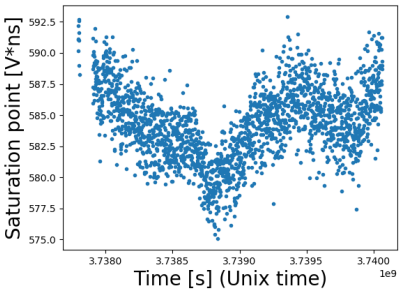

(d) Channel 3

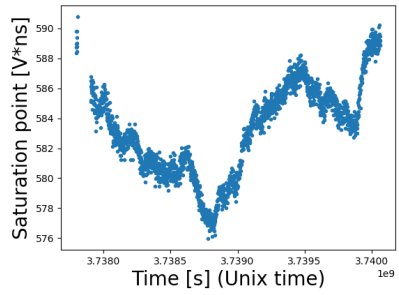

(e) Channel 4

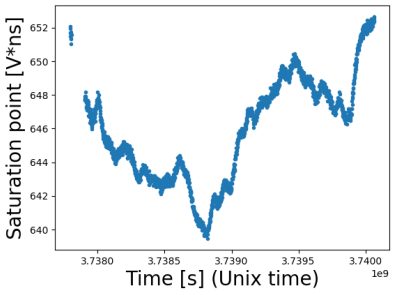

(f) Channel 5

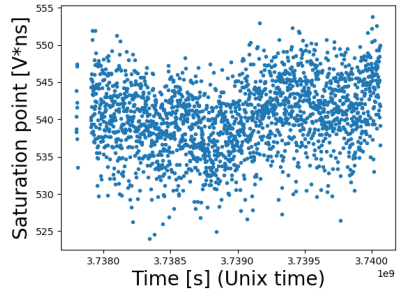

(g) Channel 6

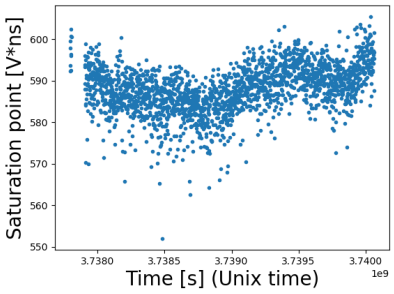

(h) Channel 7

Figure A.32: Variation of the saturation points over the time for run_2

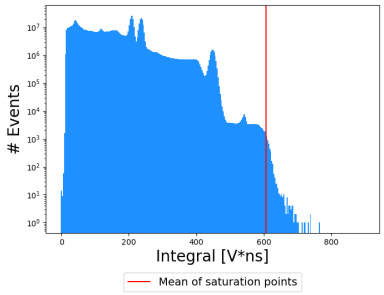

(a) Channel 0

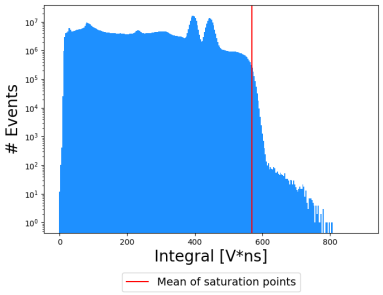

(b) Channel 1

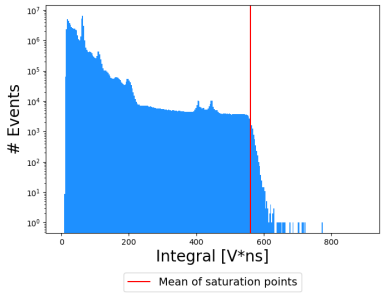

(c) Channel 2

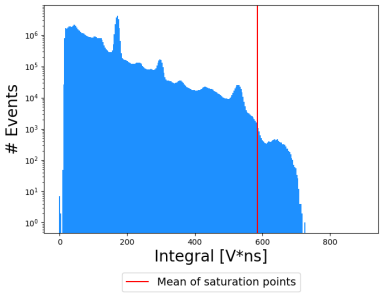

(d) Channel 3

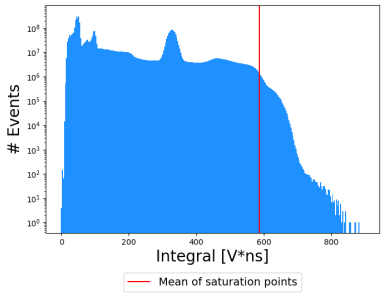

(e) Channel 4

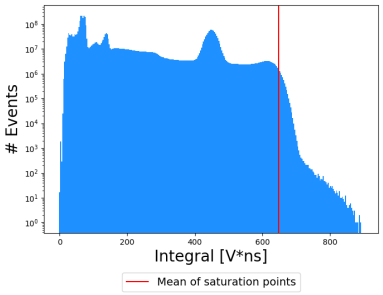

(f) Channel 5

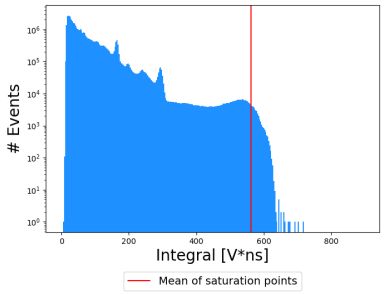

(g) Channel 6

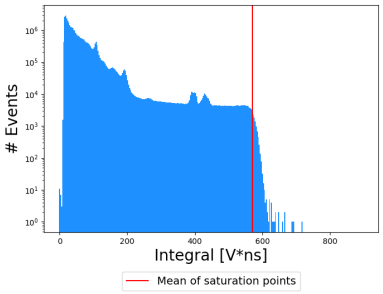

(h) Channel 7

Figure A.33: Integral spectrum of every channel with the saturation line to find saturated peaks for run_1

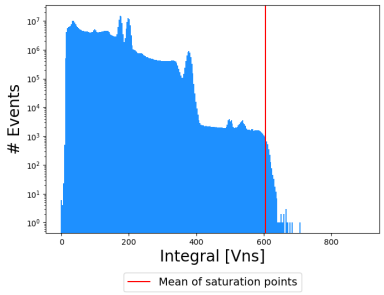

(a) Channel 0

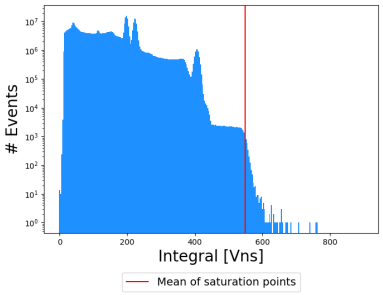

(b) Channel 1

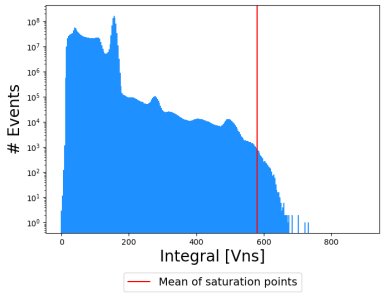

(c) Channel 2

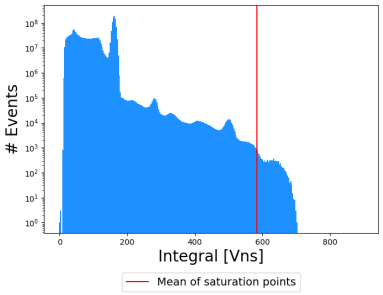

(d) Channel 3

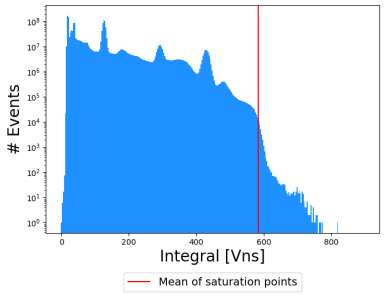

(e) Channel 4

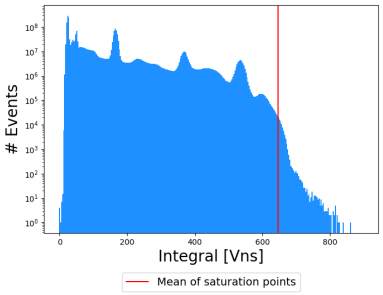

(f) Channel 5

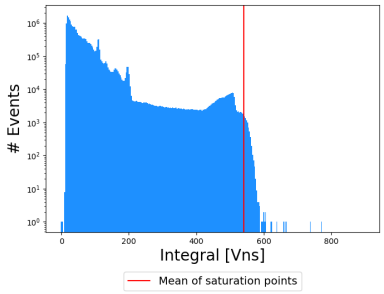

(g) Channel 6

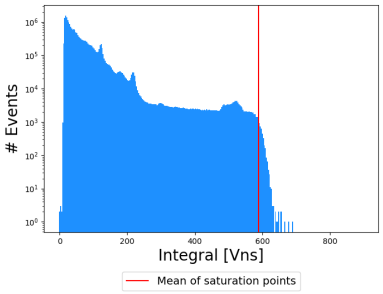

(h) Channel 7

Figure A.34: Integral spectrum of every channel with the saturation line to find saturated peaks for run_2

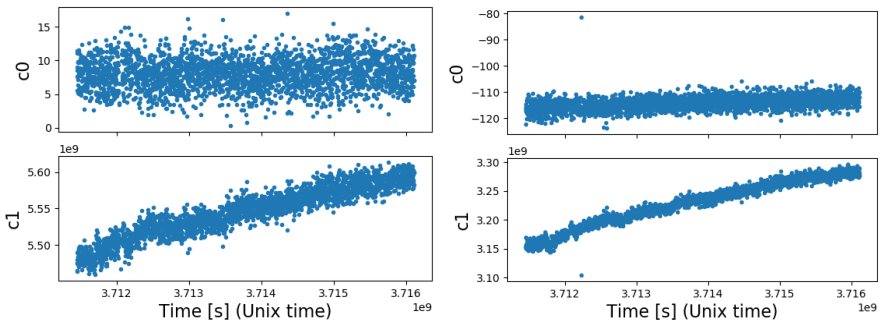

(a) Channel 0

(b) Channel 1

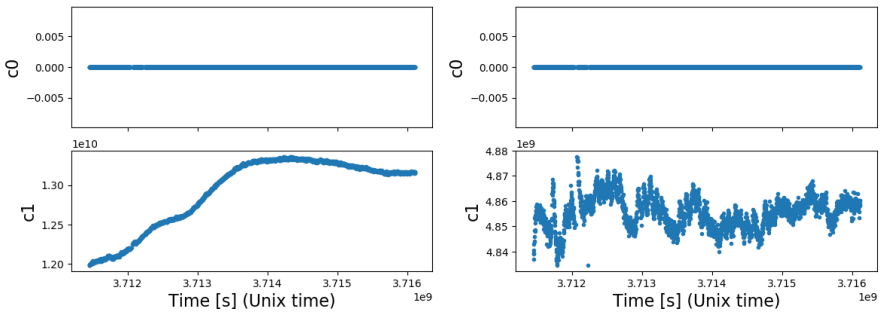

(c) Channel 2

(d) Channel 3

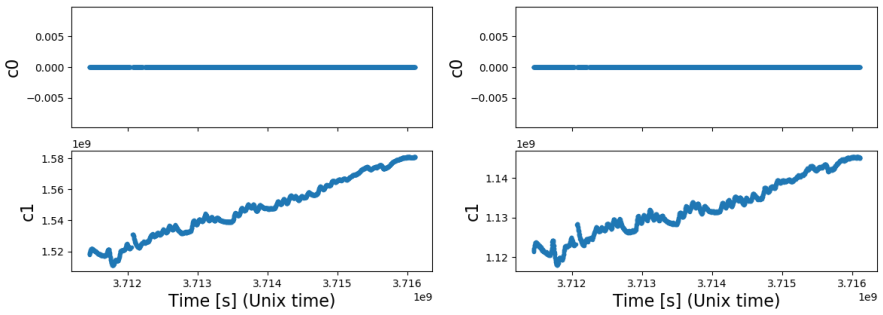

(e) Channel 4

(f) Channel 5

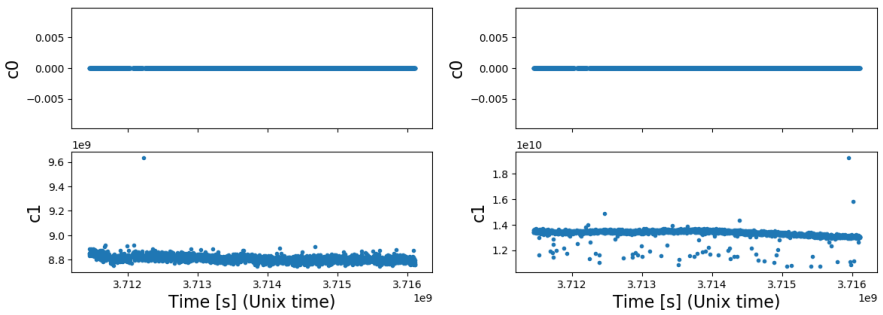

(g) Channel 6

(h) Channel 7

Figure A.35: Calibration coefficients over time for every channel in run_1

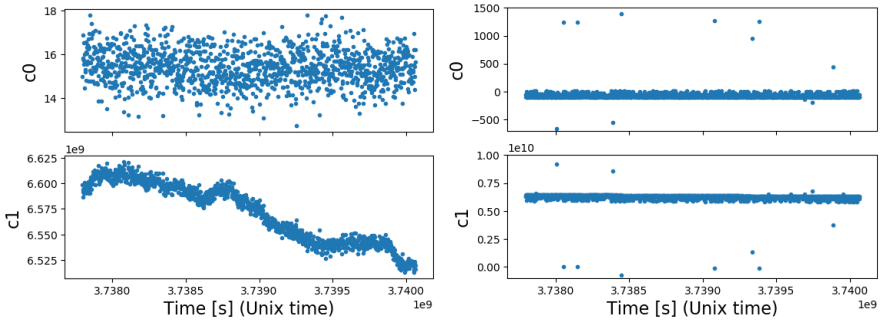

(a) Channel 0

(b) Channel 1

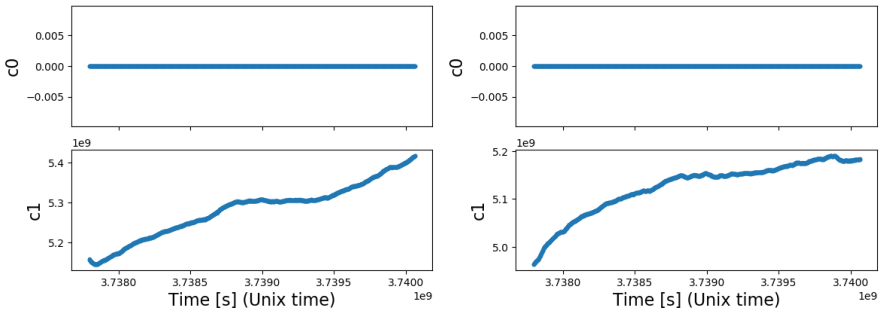

(c) Channel 2

(d) Channel 3

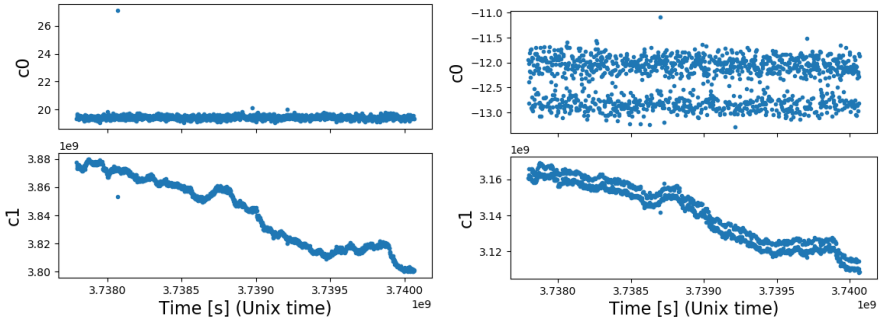

(e) Channel 4

(f) Channel 5

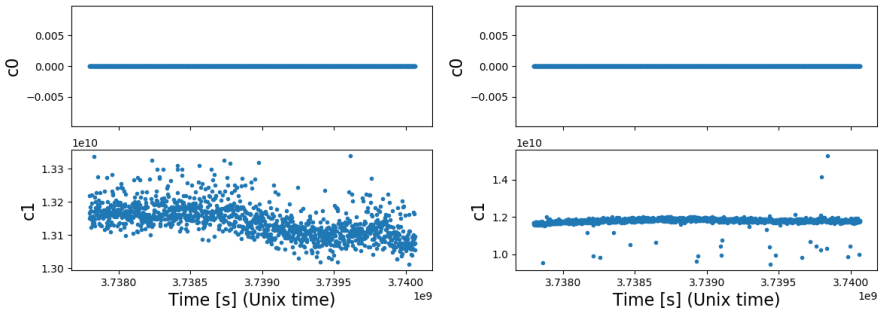

(g) Channel 6

(h) Channel 7

Figure A.36: Calibration coefficients over time for every channel in run_2

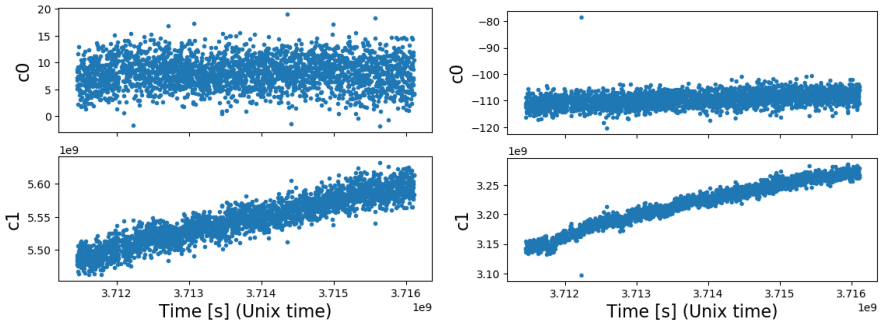

(a) Channel 0

(b) Channel 1

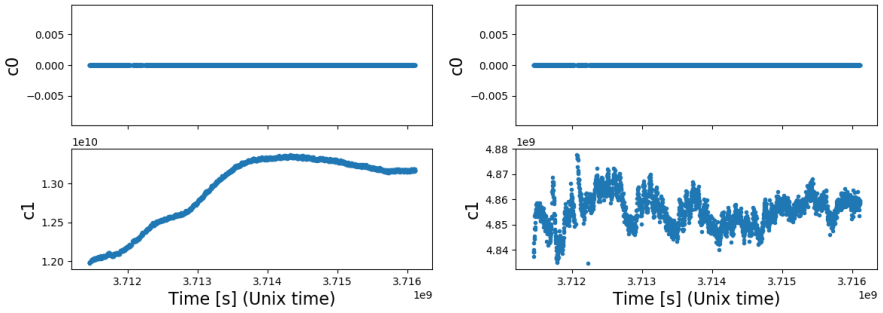

(c) Channel 2

(d) Channel 3

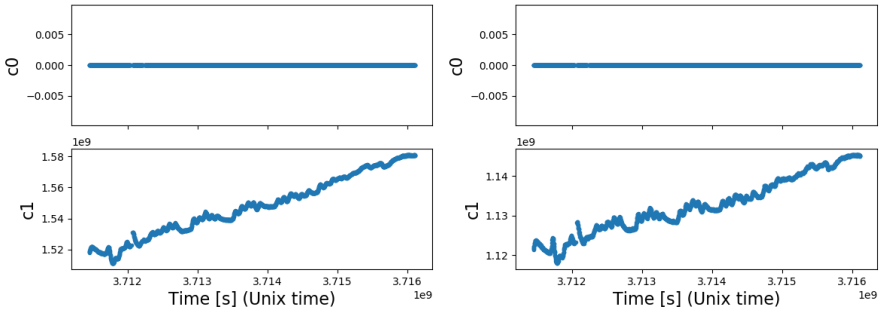

(e) Channel 4

(f) Channel 5

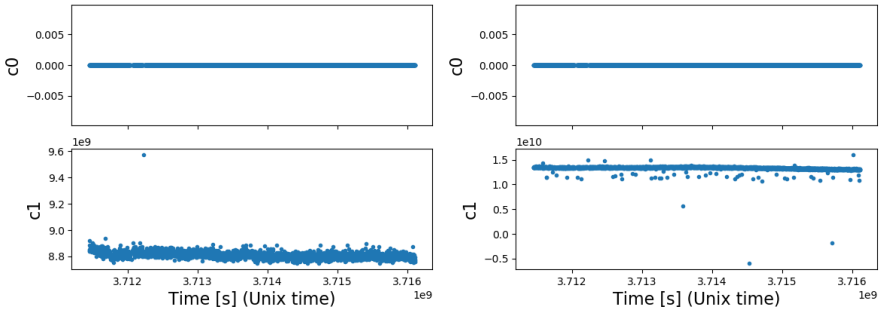

(g) Channel 6

(h) Channel 7

Figure A.37: Calibration coefficients over time for every channel in run_1 after the improvements in the calibration process

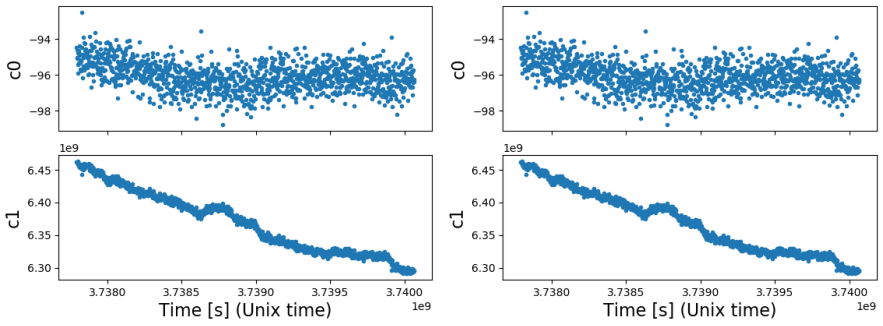

(a) Channel 0

(b) Channel 1

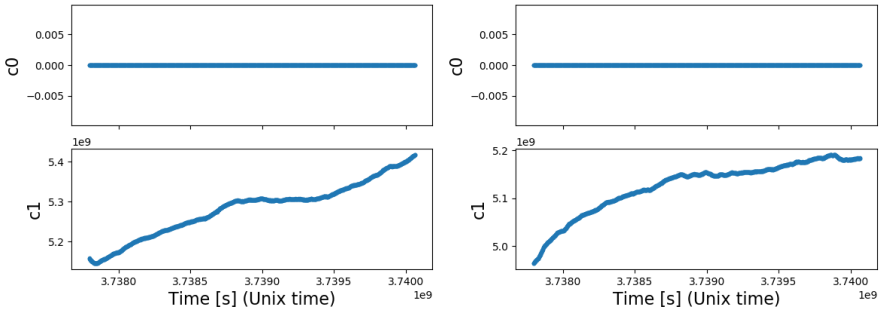

(c) Channel 2

(d) Channel 3

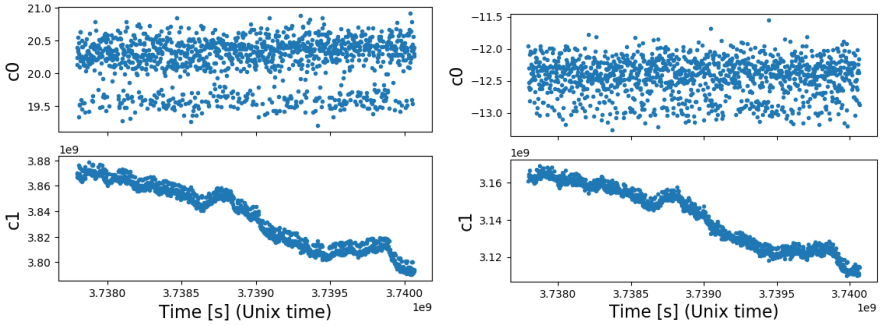

(e) Channel 4

(f) Channel 5

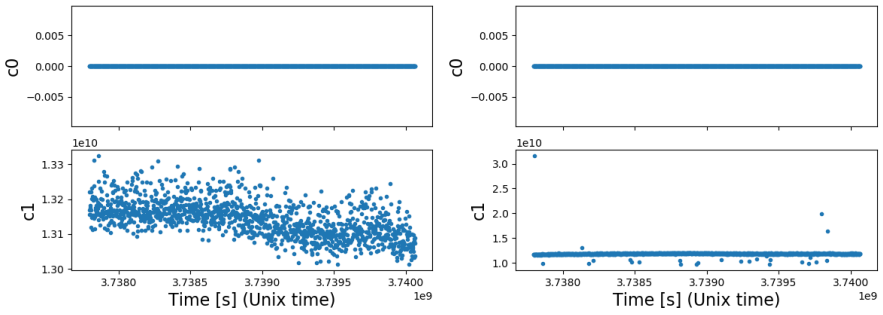

(g) Channel 6

(h) Channel 7

Figure A.38: Calibration coefficients over time for every channel in run_2 after the improvements in the calibration process

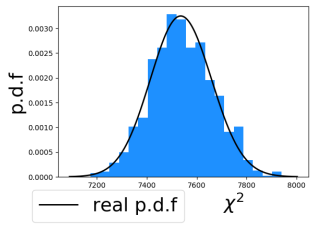

(a) chi^2 distribution of the fit result. Peak 1173.2 keV, Channel 0

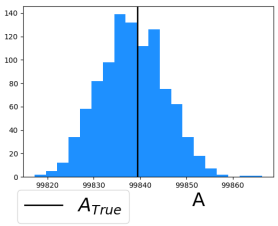

(b) Histogram of the fitted parameter A. Peak 1173.2 keV, Channel 0

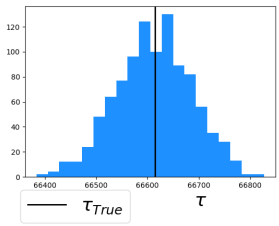

(c) Histogram of the fitted parameter τ. Peak 1173.2 keV, Channel 0

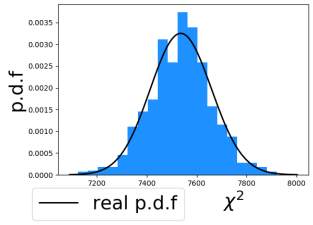

(d) chi^2 distribution of the fit result. Peak 1332.5 keV, Channel 0

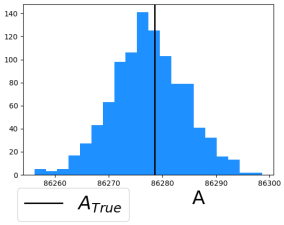

(e) Histogram of the fitted parameter A. Peak 1332.5 keV, Channel 0

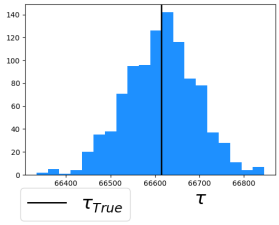

(f) Histogram of the fitted parameter τ. Peak 1332.5 keV, Channel 0

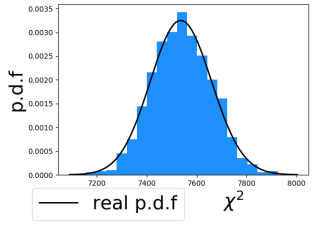

(g) chi^2 distribution of the fit result. Peak 1173.2 keV, Channel 1

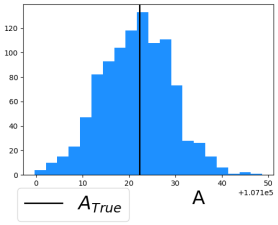

(h) Histogram of the fitted parameter A. Peak 1173.2 keV, Channel 1

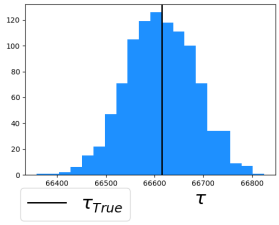

(i) Histogram of the fitted parameter τ. 1173.2 keV, Channel 1

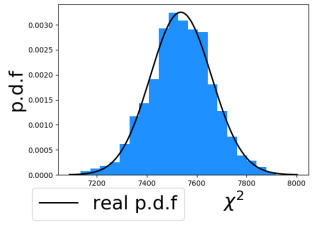

(j) chi^2 distribution of the fit result. Peak 1332.5 keV, Channel 1

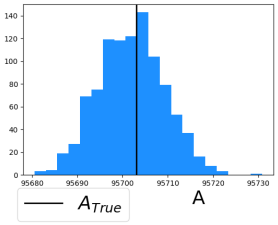

(k) Histogram of the fitted parameter A. Peak 1332.5 keV, Channel 1

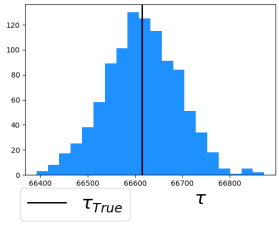

(l) Histogram of the fitted parameter τ. Peak 1332.5 keV, Channel 1

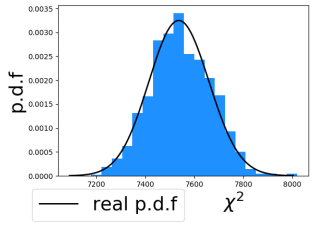

(m) chi^2 distribution of the fit result. Peak 834.8 keV, Channel 2

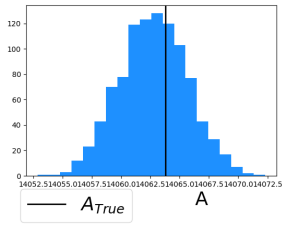

(n) Histogram of the fitted parameter A. Peak 834.8 keV, Channel 2

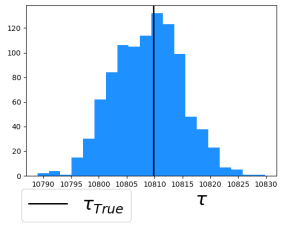

(o) Histogram of the fitted parameter τ. Peak 834.8 keV, Channel 2

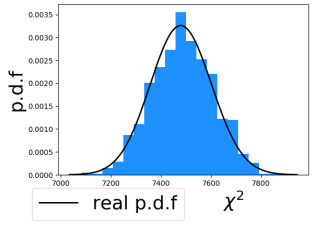

(p) chi^2 distribution of the fit result. Peak 834.8 keV, Channel 3

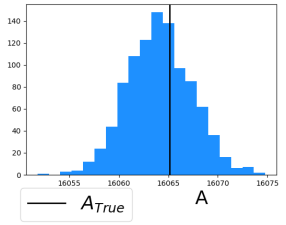

(q) Histogram of the fitted parameter A. Peak 834.8 keV, Channel 3

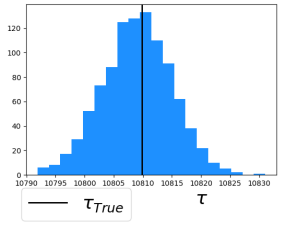

(r) Histogram of the fitted parameter τ. Peak 834.8 keV, Channel 3

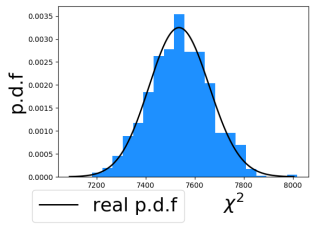

(s) chi^2 distribution of the fit result. Peak 511.00 keV, Channel 4

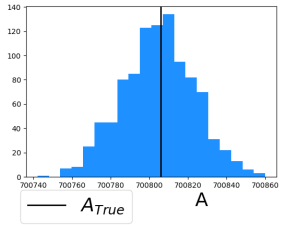

(t) Histogram of the fitted parameter A. Peak 511.00 keV, Channel 4

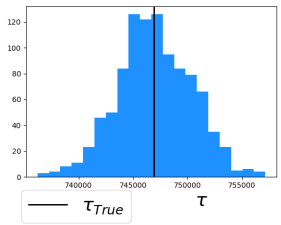

(u) Histogram of the fitted parameter τ. Peak 511.00 keV, Channel 4

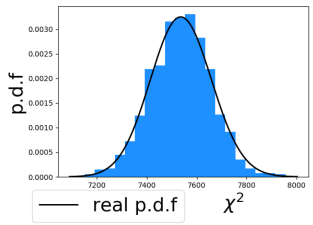

(v) chi^2 distribution of the fit result. Peak 511.00 keV, Channel 5

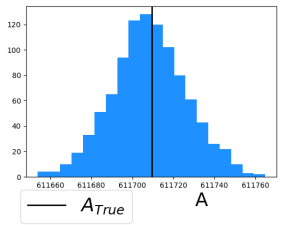

(w) Histogram of the fitted parameter A. Peak 511.00 keV, Channel 5

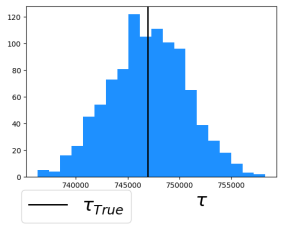

(x) Histogram of the fitted parameter τ. Peak 511.00 keV, Channel 5

Figure A.39: Fitting results of ds_0 with an exponential function.

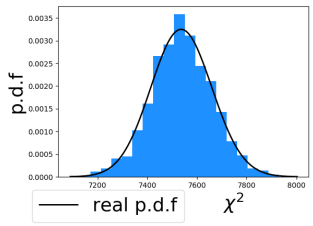

(a) chi^2 distribution of the fit result. Peak 1173.2 keV, Channel 0

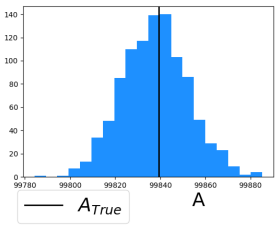

(b) Histogram of the fitted parameter A. Peak 1173.2 keV, Channel 0

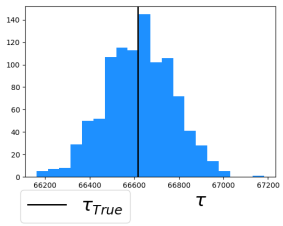

(c) Histogram of the fitted parameter τ. Peak 1173.2 keV, Channel 0

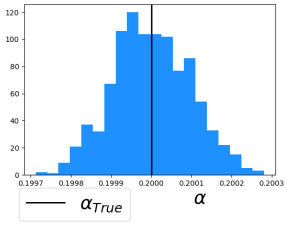

(d) Histogram of the fitted parameter α. Peak 1173.2 keV, Channel 0

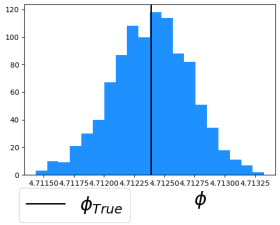

(e) Histogram of the fitted parameter ϕ. Peak 1173.2 keV, Channel 0

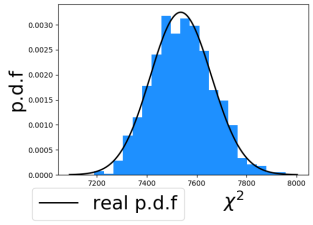

(f) chi^2 distribution of the fit result. Peak 1332.5 keV, Channel 0

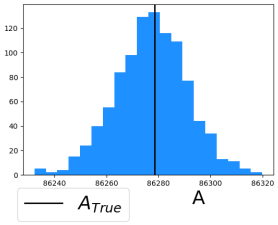

(g) Histogram of the fitted parameter A. Peak 1332.5 keV, Channel 0

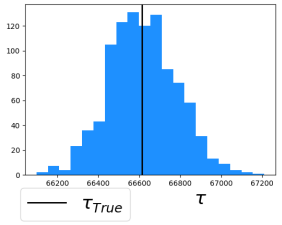

(h) Histogram of the fitted parameter τ. Peak 1332.5 keV, Channel 0

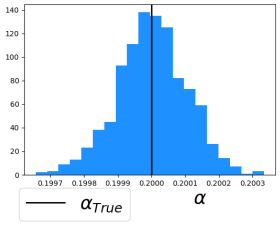

(i) Histogram of the fitted parameter α. Peak 1332.5 keV, Channel 0

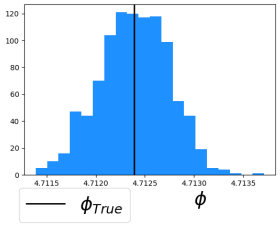

(j) Histogram of the fitted parameter ϕ. Peak 1332.5 keV, Channel 0

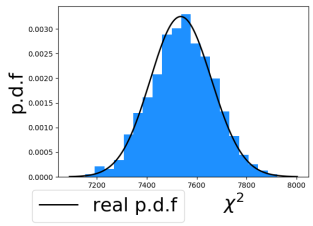

(k) chi^2 distribution of the fit result. Peak 1173.2 keV, Channel 1

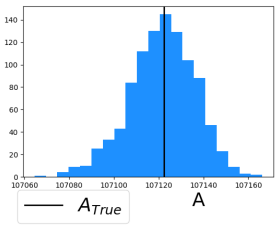

(l) Histogram of the fitted parameter A. Peak 1173.2 keV, Channel 1

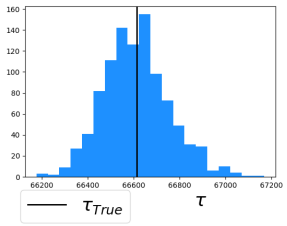

(m) Histogram of the fitted parameter τ. Peak 1173.2 keV, Channel 1

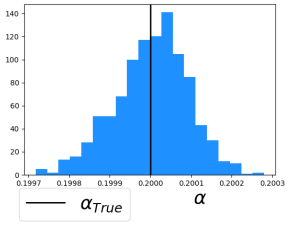

(n) Histogram of the fitted parameter α. Peak 1173.2 keV, Channel 1

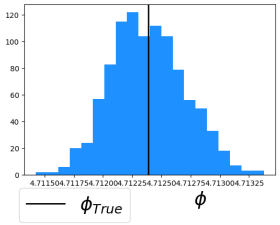

(o) Histogram of the fitted parameter ϕ. Peak 1173.2 keV, Channel 1

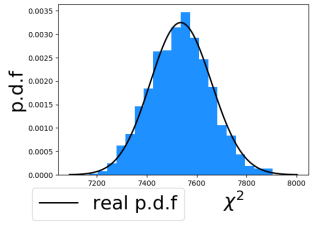

(p) chi^2 distribution of the fit result. Peak 1332.5 keV, Channel 1

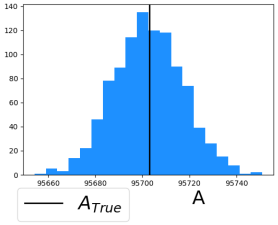

(q) Histogram of the fitted parameter A. Peak 1332.5 keV, Channel 1

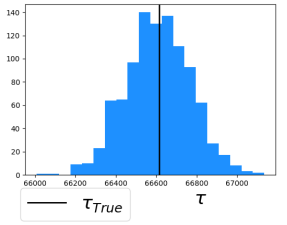

(r) Histogram of the fitted parameter τ. Peak 1332.5 keV, Channel 1

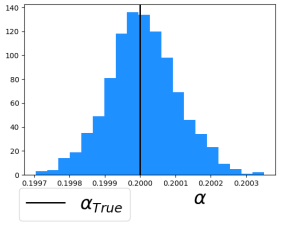

(s) Histogram of the fitted parameter α. Peak 1332.5 keV, Channel 1

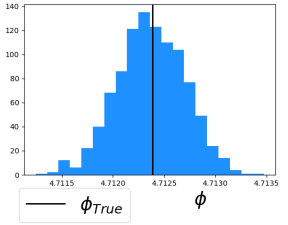

(t) Histogram of the fitted parameter ϕ. Peak 1332.5 keV, Channel 1

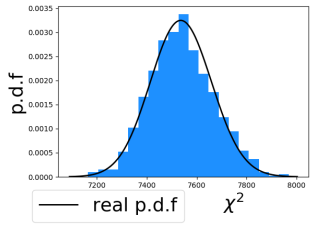

(u) chi^2 distribution of the fit result. Peak 834.8 keV, Channel 2

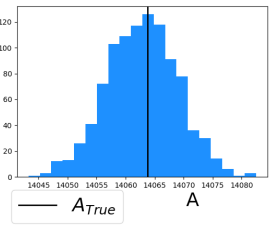

(v) Histogram of the fitted parameter A. Peak 834.8 keV, Channel 2

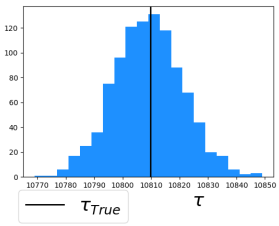

(w) Histogram of the fitted parameter τ. Peak 834.8 keV, Channel 2

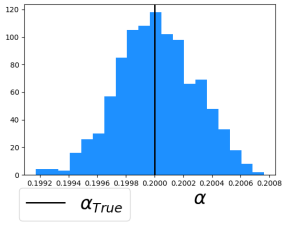

(x) Histogram of the fitted parameter α. Peak 834.8 keV, Channel 2

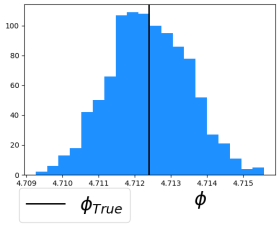

(y) Histogram of the fitted parameter ϕ. Peak 834.8 keV, Channel 2

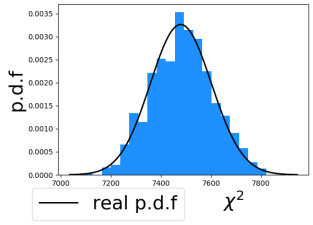

(z) chi^2 distribution of the fit result. Peak 834.8 keV, Channel 3

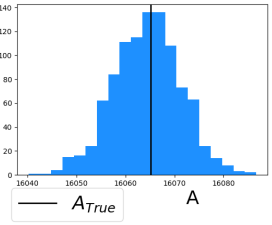

(aa) Histogram of the fitted parameter A. Peak 834.8 keV, Channel 3

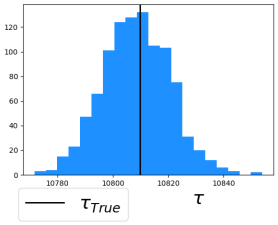

(ab) Histogram of the fitted parameter τ. Peak 834.8 keV, Channel 3

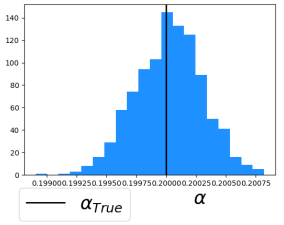

(ac) Histogram of the fitted parameter α. Peak 834.8 keV, Channel 3

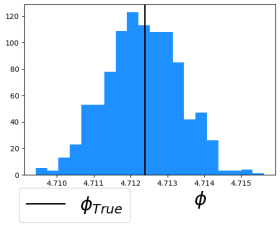

(ad) Histogram of the fitted parameter ϕ. Peak 834.8 keV, Channel 3

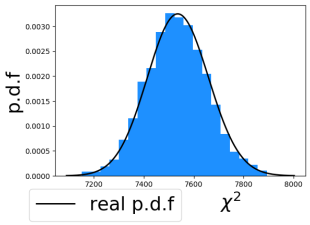

(ae) chi^2 distribution of the fit result. Peak 511.00 keV, Channel 4

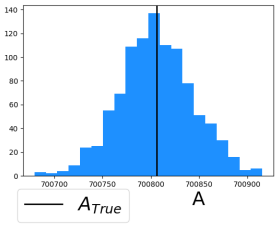

(af) Histogram of the fitted parameter A. Peak 511.00 keV, Channel 4

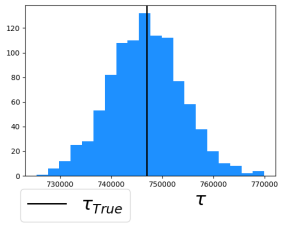

(ag) Histogram of the fitted parameter τ. Peak 511.00 keV, Channel 4

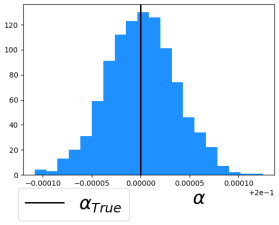

(ah) Histogram of the fitted parameter α. Peak 511.00 keV, Channel 4

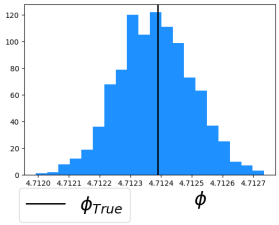

(ai) Histogram of the fitted parameter ϕ. Peak 511.00 keV, Channel 4

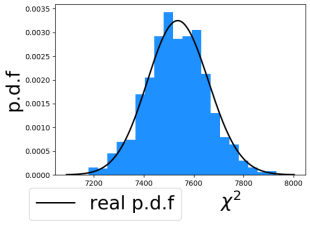

(aj) chi^2 distribution of the fit result. Peak 511.00 keV, Channel 5

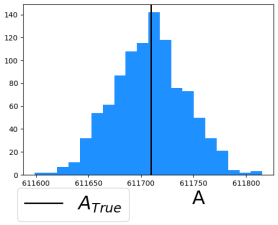

(ak) Histogram of the fitted parameter A. Peak 511.00 keV, Channel 5

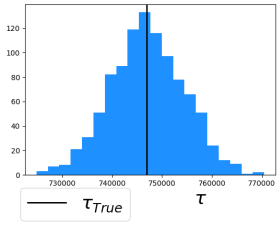

(al) Histogram of the fitted parameter τ. Peak 511.00 keV, Channel 5

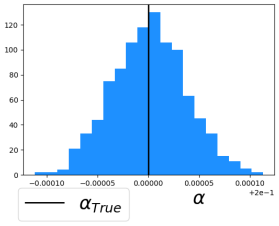

(am) Histogram of the fitted parameter α. Peak 511.00 keV, Channel 5

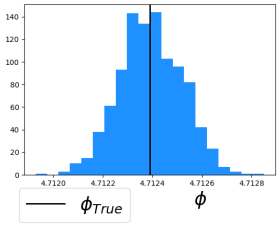

(an) Histogram of the fitted parameter ϕ. Peak 511.00 keV, Channel 5

Figure A.40: Fitting results of ds_{check} with the modulation function.

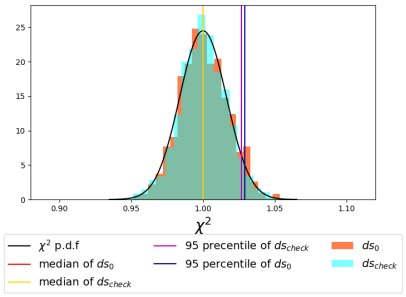

(a) Peak 1173.2 keV, Channel 0

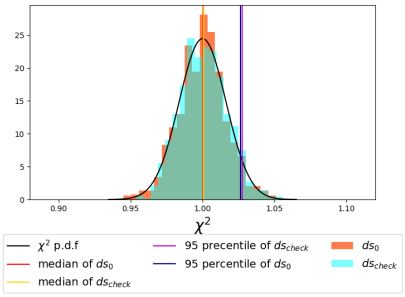

(b) Peak 1332.5 keV, Channel 0

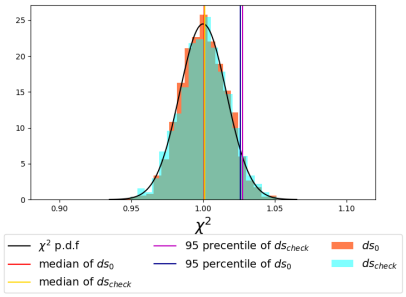

(c) Peak 1173.2 keV, Channel 1

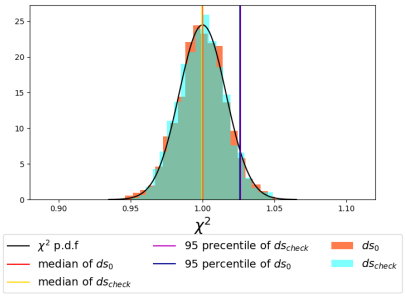

(d) Peak 1332.5 keV, Channel 1

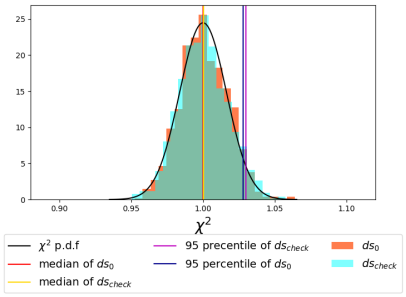

(e) Peak 834.8 keV, Channel 2

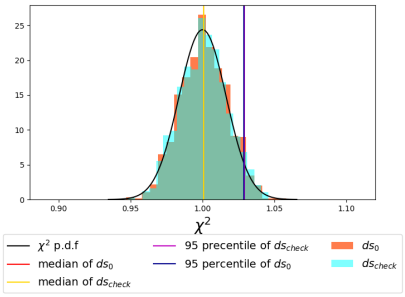

(f) Peak 834.8 keV, Channel 3

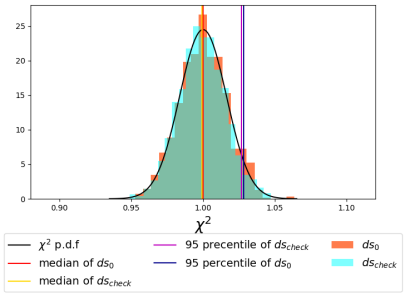

(g) Peak 511.00 keV, Channel 4

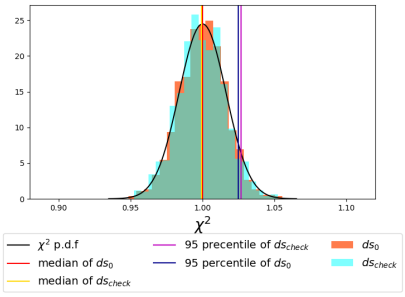

(h) Peak 511.00 keV, Channel 5

Figure A.41: Reduced χ^2 distributions of the fit of ds_0 and ds_{check} with $\alpha_{true} = \alpha_{fit}$. Also the 95 percentile and the median is shown to compare both distributions.

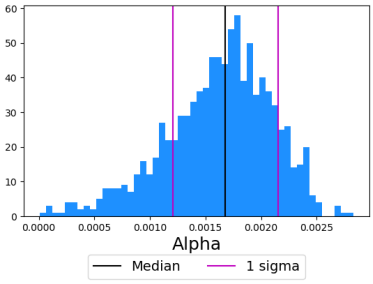

(a) Peak 1173.2 keV, Channel 0

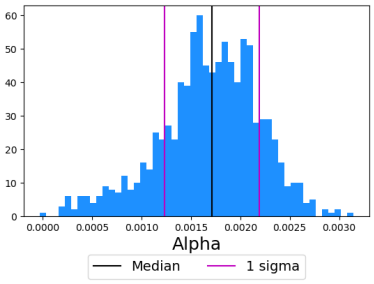

(b) Peak 1332.5 keV, Channel 0

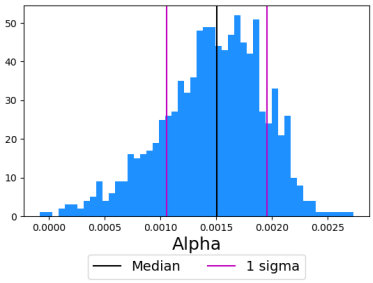

(c) Peak 1173.2 keV, Channel 1

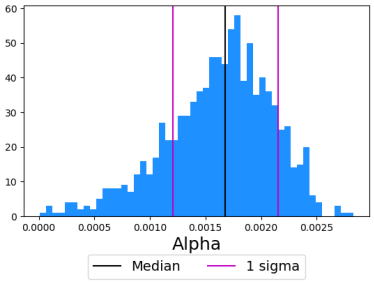

(d) Peak 1332.5 keV, Channel 1

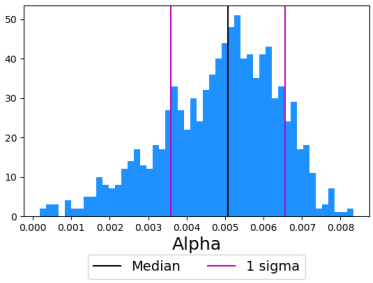

(e) Peak 834.8 keV, Channel 2

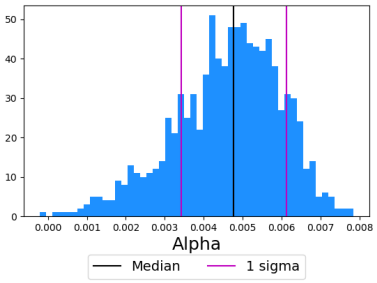

(f) Peak 834.8 keV, Channel 3

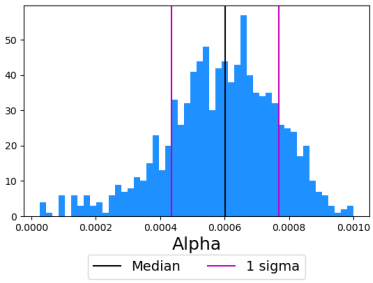

(g) Peak 511.00 keV, Channel 4

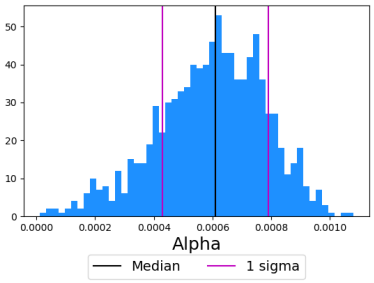

(h) Peak 511.00 keV, Channel 5

Figure A.42: Histogram of the α values which causes a χ^2 which corresponds to the 5% $P - value$. Also the standard deviation is marked which is used as statistical error.

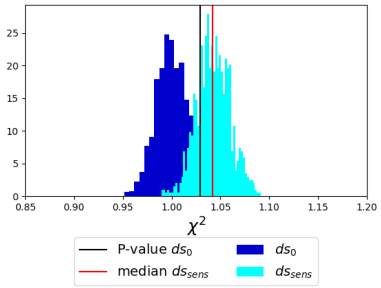

(a) Peak 1173.2 keV, Channel 0

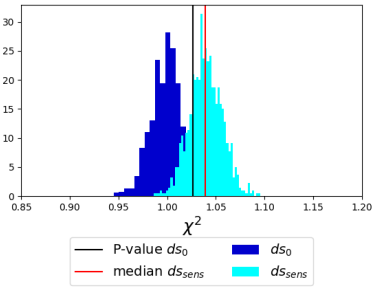

(b) Peak 1332.5 keV1, Channel 0

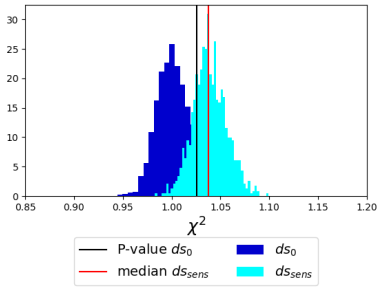

(c) Peak 1173.2 keV, Channel 1

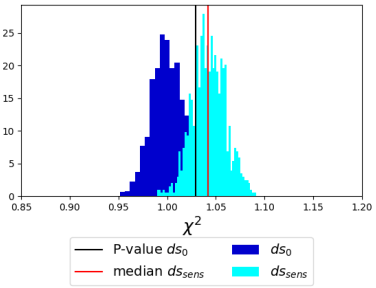

(d) Peak 1332.5 keV, Channel 1

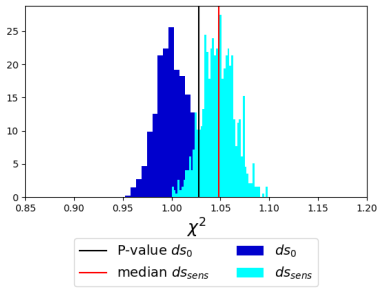

(e) Peak 834.8 keV, Channel 2

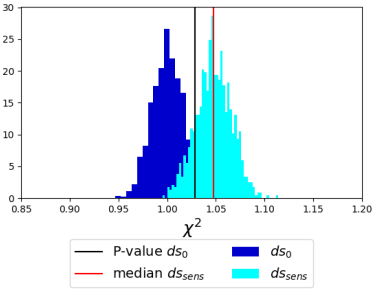

(f) Peak 834.8 keV, Channel 3

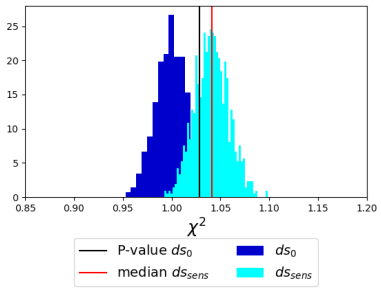

(g) Peak 511.00 keV, Channel 4

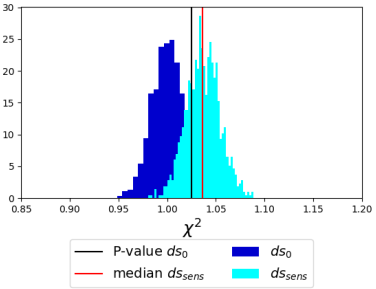

(h) Peak 511.00 keV, Channel 5

Figure A.43: The reduced χ^2 distribution of ds_0 and ds_{sens} are compared. The median of ds_{sens} should be equal to the 5% $P-value$ of ds_0. But it is a bit (<2%) shifted to the right.

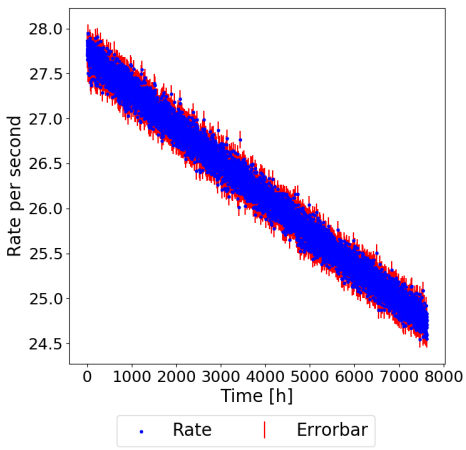

(a) Channel 0 peak 1173.2 keV

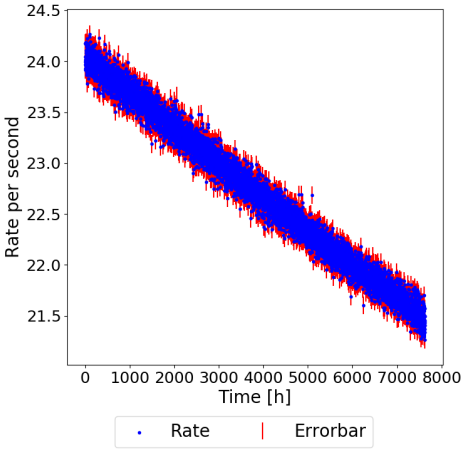

(b) Channel 0 peak 1332.5 keV

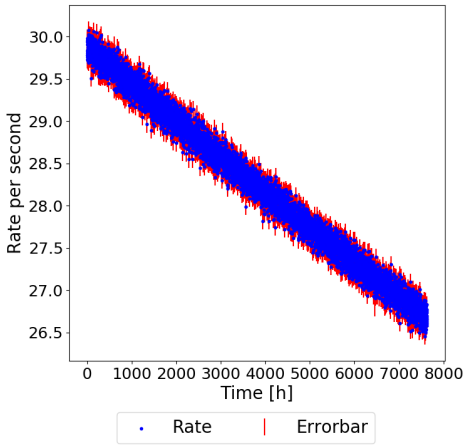

(c) Channel 1 peak 1173.2 keV

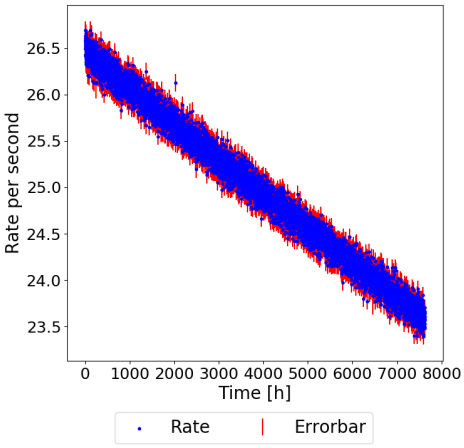

(d) Channel 1 peak 1332.5 keV

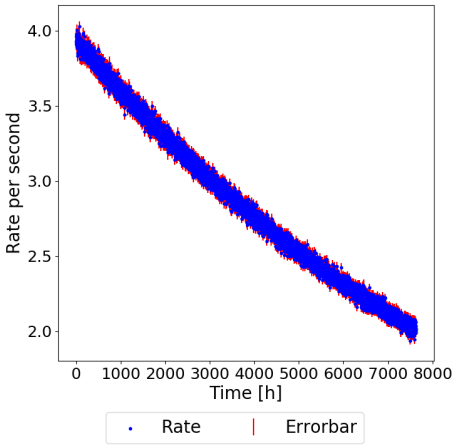

(e) Channel 2 peak 834.8 keV

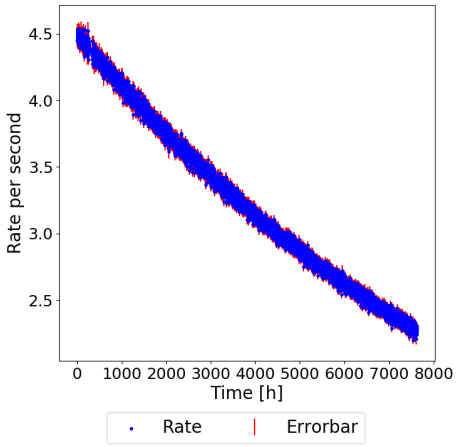

(f) Channel 3 peak 834.8 keV

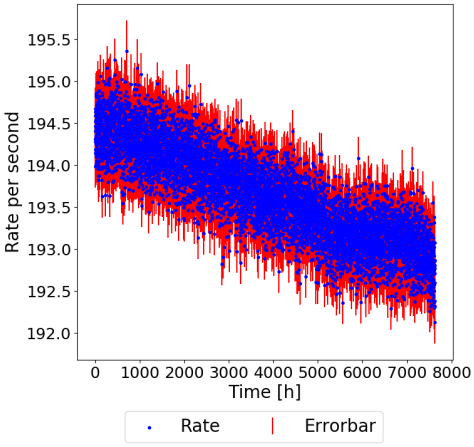

(g) Channel 4 peak 511.00 keV

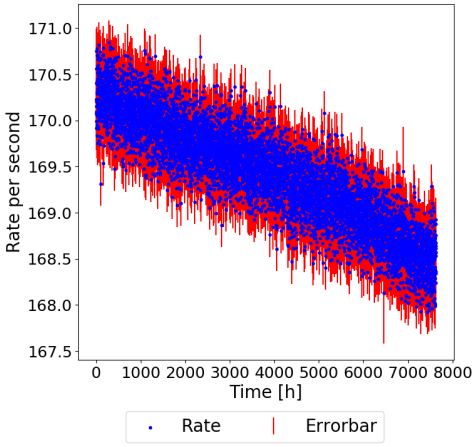

(h) Channel 5 peak 511.00 keV

Figure A.44: Rate per second without outliers for every peak and channel. These data sets are used for further analysis.